Investigating Adaptive Mesh Refinement Criteria for a Double-Distribution FMLB Scheme in Melting and Solidifaction Processes.

Thorben Besseling (4490258)

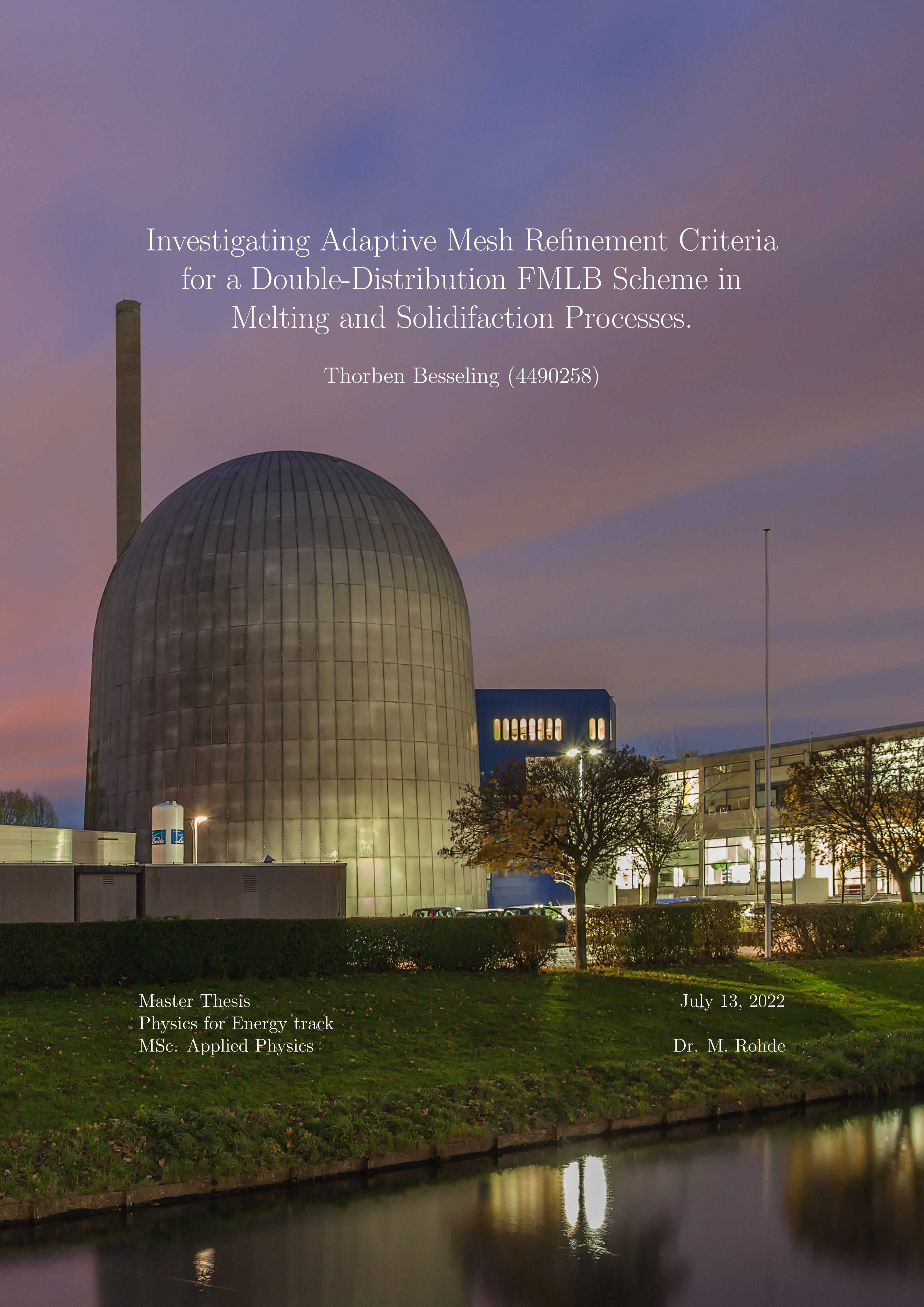

Master Thesis
Physics for Energy track
MSc. Applied Physics

July 13, 2022

Dr. M. Rohde

Abstract

The energy transition requires a mesmerizing amount of technological innovation to replace all usage of fossil fuels. One possible contendor to these solutions is the Molten Salt Reactor. It differentiates itself from the conventional Light Water Reactors by its heightened safety profile, lower waste volume with a shorter lifetime and capability to generate high temperatures which could be used in industrial applications that currently directly operate on fossil fuels.

This thesis aims to further improve modeling techniques for melting and solidification processes in flow. To this end, a double distribution Lattice Boltzmann model is used where one distribution is employed for the density and one for the enthalpy. In addition, the Filter Matrix method is used for the collision calculations. Lastly, adaptive mesh refinement is implemented to investigate the effect on accuracy and computational time.

The objectives of this thesis were: finding a computationally cheap method to implement the latent heat of melting into the filter matrix scheme, Saving computational time in simulations for the Stefan Problem and finding criteria for refinement in a convection melting problem for a rectangular cavity of gallium.

The latent heat was successfully implemented in the Filter Matrix scheme by splitting the total enthalpy in a sensible and latent heat part and only applying the collision to the sensible heat. This was verified by the simulations for the Stefan Problem and convection melting. Using the adaptive mesh refinement method the melting front in the Stefan Problem was tracked and refined. This led to a reduction in computational time of ~ 3.6 and ~ 9.9 for one and two levels of refinement.

Furthermore were two criteria for adaptive mesh refinement investigated for air convection in a square cavity: the absolute velocity and vorticity. neither led to converging solutions. The main take away is that the temperature and velocity gradients are not continuous at the interface between the coarse and fine grid.

This research was finalized by investigating the effect of different criteria for refinement on the cavity melting case of gallium. The melting front using the velocity matched poorly with the front of the purely fine grid. In contrast, using the vorticity and shear rate actually gave very similar results to the fine grid. Using the refinement led to a reduction of computational time of about 3-4 times with respect to the purely fine grid.

Acknowledgements

Allereerst wil ik graag Martin Rohde bedanken voor zijn begeleiding in dit project. Ondanks dat ik soms weinig om hulp vroeg was het erg fijn dat je altijd bereikbaar was voor vragen of gewoon een interessante brainstorm voor het whiteboard. Overigens dank voor alle goed onderbouwde feedback en adviezen om het project binnen de afgesproken termijn af te ronden. Daarnaast wil ik Anand bedanken voor zijn hulp met het installeren van software en het optimaliseren van de code. Overigens wil ik Michiel bedanken. Alle verdieping die we samen hebben uitgepluisd over kernenergie heeft me heel veel vebredeing en inzicht gegeven over het grotere geheel van dit onderzoek. De boeiende momenten daarin waren uiteraard de scherpe vragen die we altijd kregen bij onze presentatie tour.

Het onderzoek doen op het RID is altijd heel goed bevallen. Momenten als de gezamenlijke lunches, team meetings en espresso-sinaasappelsap proeverij waren een basis voor een fijne werksfeer. Ookal had dat laatste ook best een normale kop koffie mogen zijn. Overigens dank aan Richard voor de alle adviezen over coderen tijdens onze overdagse bouldersessies. Wanneer ik tegen een nare bug aanliep was het altijd fijn even twee uurtjes een break te hebben en m'n hoofd totaal leeg te maken. Hierbij wil ik ook mijn vrienden bedanken voor alle mooie festivals en lange uitgaansnachten in Rotterdam. Niet altijd goed voor de mentale helderheid, maar wel voor de nodige uitlaatklep in deze stressvolle periode.

Mama, Sybe en Ward, jullie wil ik in het voornaamste bedanken voor alle steun en begrip die jullie me altijd hebben geboden gedurende deze hele weg. Ik ben jullie dankbaar voor jullie mooie momenten samen, in het speciaal de vakantie samen met Marrissa en Esben. Fijn dat dat na al die jaren eindelijk weer kon.

Thorben Besseling, 1 juli 2022

Contents

1 Introduction

This section will cover the scope of the research, starting with some background on nuclear energy: the use case, historic developments and new generation of reactors, with special attention to the molten salt reactor. This thesis aims to improve modeling on the melting and solidification processes in the presence of flow in contribution to the further development of modeling the salt in the molten salt reactor. Particular subjects of interests that require such models are e.g. the start-up/shut-down procedure and the freeze plug [44], which sits at the bottom of the first containment vessel and melts upon overheating causing the fuel to a flow down to non-moderated emergency dump tank.

1.1 The Need for Nuclear Energy

Nuclear energy production is considered to be a necessity in reducing carbon dioxide, CO_2, emissions. *The Intergovernmental Panel on Climate Change*, IPCC, argues that plausible scenarios for limiting warming to a maximum of 1.5 degrees depend on electrification of energy end use [39]. This means that current applications of fossil fuels should be replaced by electric alternatives. For instance, electric vehicles replacing conventional vehicles powered by internal combustion engines. This will, however, lead to an increased demand for electricity. Currently, the global demand compromises nearly 20% of total energy consumption and is expected to grow to 40-60% [6]. The IPCC elaborates that the potential growth in renewable energy production is too slow to meet the demand for low carbon energy sources. To meet this demand, an increase in nuclear power production is proposed in all four of the IPCC's scenerios. [6].

The potential electricity supply from nuclear power is increasing. Currently, there are approximately 50 reactors under construction globally. The majority of growth in the upcoming decades is expected to arise from the installment of Generation III reactors, among these mainly *Pressurized Water Reactors*, PWRs, and *Boiling Water Reactors*, BWRs [36].

When it comes to construction of new *Nuclear Power Plants*, NPPs, there are major public concerns. These include, but are not limited to: a nuclear disaster such a Chernobyl 1986, the potential leakage of radioactive nuclear waste, weapon proliferation, a long planning to operation time.

Besides political challenges does advancement in nuclear energy also face technological challenges. Although the reactors under construction today are, by any means, much safer than the one in Chernobyl and the *Boiling Water Reactors* and *Pressurized Water Reactors* from Generation I and II, there is still a lot of ongoing research for new reactor designs. Besides advancements in safety, future types of reactors have to potential to, for instance, produce radioactive waste with a shorter half-life and be more cost effective in producing electricity. Currently, the estimated levelized cost of electricity produced by NPPs is still higher (between 6.5 and 12 ct/kWh) than other low-carbon sources, such as wind and solar [36].

1.2 Generations of Nuclear Reactors.

In 1951, the first nuclear reactor was created that would successfully generate electricity. This was the Experimental Breeder Reactor I in Idaho, USA. It was called as such as it was designed to create more fissile material than it consumed. Later this era, the first commercial NPPs were installed [41]. In the upcoming years, NPPs were constructed for commercial and or military use. These reactors are classified as Generation I reactors which were early prototypes. Among these these were the Gas Cooled Reactor "Magnox", UK; the Shippingport PWR reactor, PA, USA; Wylfa, Wales; CANDU-137, Pakistan. The last of which is the only first generation reactor still in operation [33].

Generation II reactors differentiate themselves from the first generation by safety features in their design. Additionally, are these reactors more economical and more dependable, making them suitable for commercial use. These usually are *Ligth Water Reactors*, LWRs. The first second generation reactors were built in the 1960's and the majority of todays LWRs belong to this generation [16].

The third generation, Generation III, reactors are improved versions of the former generation. With regard to safety, are they equipped with more reliable systems, especially automatic features. These automatic features are intended to stop the reaction without any human input involved in case of an accident. Other advancements are in: fuel technology, efficiency, modular construction, lifetime of operation and the standardization of designs [16]. The latter of which has a beneficial effect on development costs.

1.2.1 Future Reactors

The future designs of nuclear reactors are the so called Generation IV reactors. In 2001 the *Generation IV International Forum*, GIF, was established for international cooperation on research and development [54]. The GIF selected six contenders for the future Generation IV reactors as the most promising. These reactors are destined to use advanced fuels and have a high burn-up rate. In addition, they feature enhancements in safety and reliability.

The six types of reactors are: the *Gas-cooled Fast Reactor*, GFR; *Lead-cooled Fast Reactor*, LFR; *Molten Salt Reactor*, MSR; *Supercritical Water-cooled Reactor*, SCWR; *Sodium-cooled Fast Reactor*, SFR and the *Very High Temperature Reactor*, VHTR [15].

1.2.2 Molten Salt Fast Reactor

This research is focused one of these proposed designs, the MSFR. In the MSFR the nuclear fuel is in solution in a liquid fluoride or chloride salt. A depiction of the MSFR is given in Figure 1.1. In the plant one can see the flow cycle of the fuel. This consists of the reactor itself, the heat exchanger to the coolant salt and the chemical processing plant to purify the salt. The latter allows the fuel to be purified on-site. Currently there is still a lot of research required to prove the safety and feasibility of this reactor.

Together with other universities and research institutes, the TUDelft is part of the SAMOSAFER consortium. One of the aims of the SAMOSAFER is to prove the safety of the MFSR through experimental and numerical research. One of the investigated safety features is the freeze plug, as a part of the emergency draining system (EDS), which is situated at the bottom of the reactor vessel and melts upon overheating of the reactor. This plug should melt within a matter of minutes to prevent the reactor's temperature from rising excessively [35] in case of a power outage.

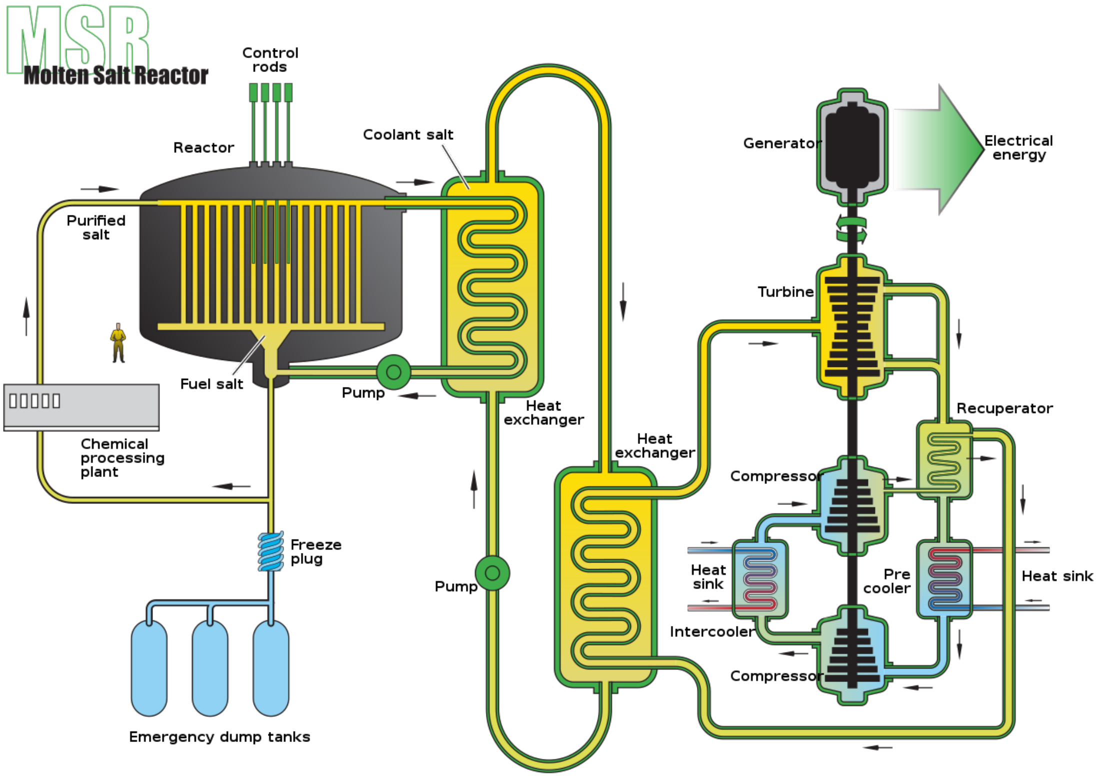

Figure 1.1: Schematic overview of a Molten Salt Reactor [27]

1.3 Fluid Dynamics Simulations

The are various options for modeling fluid dynamics in nuclear plants. Safety assessments on light water reactors are often performed with the use of so called ”system codes” [7]. In this code a fluid domain, like a pipe, is split into very coarse cells in which the thermal hydraulic processes are calculated. These models can however not capture our interest in this thesis: the localized melting and solidification processes as the cells are so coarse.

Various computational fluid dynamics (CFD) codes already exist. These models aims to solve the Navier-Stokes equations on the mesoscopic scale since microscopic particle behaviour does often hardly affect a fluid system [46]. Currently there are already some solvers which could be used directly such as OpenFOAM [30], COMSOL [8] and ANSYS [2]. The advantage is that these codes are mostly pre-build, meaning that that the user can work from an existing validated code. However, do these codes lack modularity which means that expanding or editing is complicated.

The Lattice Boltzmann model (LB) is in contrast very modular due to it simple calculation procedure. In addition, is this method very suitable for parallelization and implementing complex geometries [14]. This thesis aims to further improve LB modeling for melting and solidification processes with the bigger scope of analyzing the thermohydraulics of the molten salt.

In previous work by van Winden [48] a Lattice Boltzmann model was used for the flow field and a finite difference scheme for the temperature field. When modeling melting of gallium by thermal diffusion in one dimension, i.e. the Stefan-problem, the results were comparable to the analytical solution. This model was then used to simulate octadecane melting with a high Prandtl number of 50. The results were in reasonable agreement with other literature, however, the model exaggerates the effect of natural convection in comparison with the benchmark case. This model was also tested in a low Prandtl substance, gallium. In the simulation of the melting of this substance, severe instabilities arose. The model was found to contain a bug which makes these results unreliable.

The model for this research will be a double distribution Lattice Boltzmann model; one distribution for the momentum field and one for the thermal field. Currently double distribution melting models are limited to single, double [13] and multiple [20] relaxation time schemes. The first two models are known for possible numerical diffusion along at the phase change region [26, 17].In a benchmark test for Rayleigh-Bénard convection the MRT method has shown to be numerically stable for Rayleigh numbers up to 10^8 [20] in a 2D cavity with a MRT scheme for both distributions. For melting problems of low Prandtl substances the double MRT model seemed to be in agreement with experimental data and other numerical models for Rayleigh number in the order of 10^6, [24, 51].

The downside of MRT model is its dependency on the selection of a set of free parameters which can significantly influence the accuracy and stability of results [52]. In MRT physical moments are relaxed by a relaxation time. However, there is no accurate way to determine by what relaxation time these physical moments ought to be relaxed [49]. Another disadvantage of the MRT method is that simulations with high Reynolds numbers require very fine grids, since using small viscosities conveys stability issues [45].

For those reasons this thesis dedicated to the "Filter Matrix Lattice Boltzmann" (FMLB) method. Unlike SRT, TRT and MRT models the collision model is nonlinear [52]. In the FMLB model flow parameters are solved with the involvement of two free parameters that damp higher order terms. The FMLB scheme does not seem to strongly depend on these damping coefficients [52]. One downside of FMLB compared to MRT is that the FLMB scheme requires two 9×9 matrix-vector multiplications instead of one to perform the collision step, which makes it more expensive.

1.3.1 Phase Change Modeling

One issue that ensues from using the FMLB model is the implementation of the melting. Currently, no models exist for the implementation of the latent heat of melting in FMLB, which creates a discontinuity in the enthalpy-temperature dependence. In previous literature for the calculations of the temperature the source based enthalphy method or linearized enthalpy method were employed [40]. These methods require an iterative process to solve for the temperature [48]. In the double distribution model, these methods can be used as well to obtain stable calculations [5, 22]. The source based method can, however, be implemented without an iterative process. One option is to incorporate the latent heat source term into the distribution of the temperature [10], which requires to solve a set of linear equations. Another option is to modify the equilibrium distribution of the temperature field and implicitly account for the latent heat source term [18]. This is probably even less expensive since it does not require to solve a set of equations. This thesis aims to efficiently implement the latent heat source term; without iterative schemes as these are expensive.

1.3.2 Adaptive Mesh Refinement

One of the complexities that are complementary with fluid dynamic is that coarse grid might not be able to capture the physical processes, since certain parts of the domain might require a finer grid. In 2D LB models the computational expense increases by the power of four with respect to the grid fineness. Ergo, refining only those regions of the mesh that require fineness may save a lot of computational expense whilst possibly making to compromise on accuracy and stability. Hence, this method is also explored in this thesis.

1.3.3 Approach

In order to test these methods benchmark cases are evaluated. The first one is the Stefan Problem where the phase change region is refined, the second is natural convection of air in a square cavity where refinement dependent on the vorticity is compared to refinement based on the absolute velocity. And lastly the melting of gallium in a square cavity is simulated.

In conclusion, this brings us to the following research questions:

- How can the source based method be implemented in a termal FMLB scheme?
- To what extend does adaptive mesh refinement reduce computational expense in simulating the Stefan Problem?
- How can adaptive mesh refinement be implemented for convection melting?
- How does this influence the results?

2 Theory

This section will explain the key theoretical concepts necessary to understand the Lattice Boltzmann method and the Filter Matrix method for the collision operator.

2.1 Diffusion Advection Problem

The simulation aims to solve the Navier-Stokes equations for momentum mass transfer in the incompressible limit in conjunction with the diffusion advection Equation for heat transfer. The continuity equatuion for mass is given by Equation 2.1

$$\frac{\partial \rho}{\partial t} + \nabla \cdot (\rho \vec{u}) = 0, \tag{2.1}$$

where $\vec{u}$ is the velocity of the fluid, t the time and ρ the density. For incompressibility this reduces to $\vec{\nabla} \cdot \vec{u} = 0$. Equation 2.2 specifies the momentum conservation [32]:

$$\rho \frac{\partial \vec{u}}{\partial t} + \rho(\vec{u} \cdot \vec{\nabla})\vec{u} = \rho \vec{g}_{grav} - \vec{\nabla} p + \nu \rho \vec{\nabla}^2 \vec{u}, \tag{2.2}$$

where $\vec{g}_{grav}$ the applied body force; gravitational acceleration, p the pressure and ν the viscosity, which is considered a constant.

In buoyancy driven flow the Boussinesq approximation is often applied, where the density is considered to e a function of temperature instead of temperature and pressure [32]. Aditionally, should the the relative thermal expansion be small, as shown in Equation 2.3:

$$\beta_{exp}(T - T_0) \ll 1, \tag{2.3}$$

where β_{exp} is the thermal expansion coefficient and T_0 is the mean of the coldest and the hottest part of the fluid. Equation 2.4 approximates the density-temperature dependence through the Boussinesq approximation [38]:

$$\rho = \rho_0 - \rho_0 \beta_{exp}(T - T_0), \tag{2.4}$$

where ρ_0 is the average density of the fluid. Equation 2.2 is modified to Eqaution 2.5:

$$\frac{\partial \vec{u}}{\partial t} + (\vec{u} \cdot \vec{\nabla})\vec{u} = -\frac{1}{\rho_0} \vec{\nabla}(p + \vec{g}_{grav} \cdot \hat{z}) + \nu \vec{\nabla}^2 \vec{u} - \vec{g}_{grav} \beta_{exp}(T - T_0). \tag{2.5}$$

Where the last term gives the thermal bouyancy force in the Boussinesq approximation.

The transport of heat is described by the first law of thermodynamics, as given by Equation 2.6 [4]. Here C_p is the heat capacity of the material, taken as a constant; α the thermal diffusivity, also considered to be constant; $\rho\nu D_{viscous}$ the viscous heat dissipation, considered to be zero and Φ a source term.

$$\rho C_p \frac{\partial T}{\partial t} = \nabla \cdot (\alpha \nabla T) + \beta_{exp} T \frac{\partial p}{\partial t} + \rho\nu D_{viscous} + \Phi \tag{2.6}$$

2.1.1 Melting and Solidification

In this thesis the melting and solidification of fluid is covered for convective flow. Upon the melting of the solid or liquid fuel latent heat is absorbed/released. This heat can be implemented as the source term, Φ [W/m^3], in the heat equation which represent the rate of change in latent heat. Under the conditions that the thermal diffusivity is a constant, that there is no viscous heat dissipation and that the compressibility effect is negligible, Equation 2.6 reduces to Equation 2.7:

$$\frac{\partial T}{\partial t} + \vec{u} \cdot \vec{\nabla} T = \alpha \vec{\nabla}^2 T + \frac{\Phi}{\rho C_p}. \tag{2.7}$$

2.2 Lattice Boltzmann Method

The Lattice Boltzmann method is used in CFD (Computational Fluid Dynamics) to solve the Navier-Stokes equations through a discretization of momentum, time and space. In the scheme, particles are imagined as positioned on a certain point in a lattice with a certain velocity in the direction towards another adjacent lattice point. In 2 dimensions one could use the so called "D2Q9" lattice, which implies 2 dimensions and 9 directions. The first one being the stationary, no momentum, and the other 8 the directions of the adjacent points in the orthohormbic lattice, see Figure 2.1. Here the vectors $\vec{c_0}$ through $\vec{c_8}$ represent the discrete velocities of the distributions, given by Equation 2.8 [42].

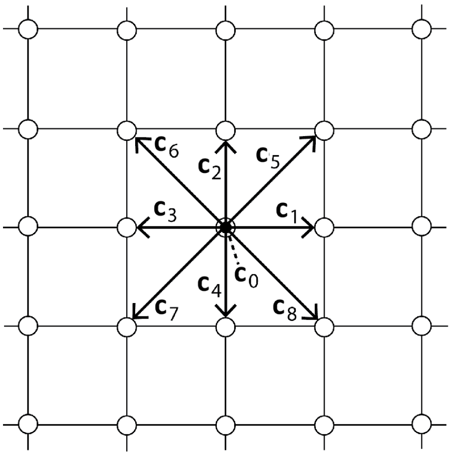

Figure 2.1: Discretization in a D2Q9 lattice [37]. The vectors $\vec{c_1}$ through $\vec{c_8}$ represent the steps to adjecent lattice nodes.

$$\vec{c_i} = \begin{cases} (0,0) & i = 0 \\ c(\cos[(i-1)\pi/2], \sin[(i-1)\pi/2]) & i = 1,2,3,4 \\ \sqrt{2}c(\cos[(2i-9)\pi/4], \sin[(2i-9)\pi/4]) & i = 5,6,7,8, \end{cases} \tag{2.8}$$

where c is the lattice speed. Which is characterized by the magnitude of the lattice spacing, Δx, and the time step, Δt, by $c = \Delta x/\Delta t$.

In the simulation each point in the lattice is described by these nine distributions, f_i, which represent the particle density moving in that direction. The sum of these represents the density, ρ on the given point, see Equation 2.9.

$$\rho(\vec{x}, t) = \sum_i f_i(\vec{x}, t), \tag{2.9}$$

where $\vec{x}$ and t refer to a specific point on the lattice on a specific point in time.

In the Lattice Boltzmann scheme density and momentum are related by the fact that these distributions also add up to the total momentum if the directions of the velocity of these distributions are taken into account, see Equation 2.10.

$$\rho\vec{u}(\vec{x}, t) = \sum_i \vec{c_i} f_i(\vec{x}, t), \tag{2.10}$$

where $\vec{u}(\vec{x}, t)$ is the nett velocity.

In general the Lattice Boltzmann scheme consists of two steps: *streaming* and *collision*, see Figure 2.2. During the streaming step particles move to the lattice point in line with the extension of their direction. In other words, the distributions move to a new lattice point. Which is formulated by Equation 2.11:

$$f_i\left(\vec{x} + \vec{c_i}\Delta t, t + \Delta t\right) = f_i(\vec{x}, t). \tag{2.11}$$

This step also takes into account the specified boundary conditions.

The collision step simulates the interaction of the particles and performs a relaxation on the distribution. There many ways to implement this. The chosen implementation is explained in Section 2.2.1.

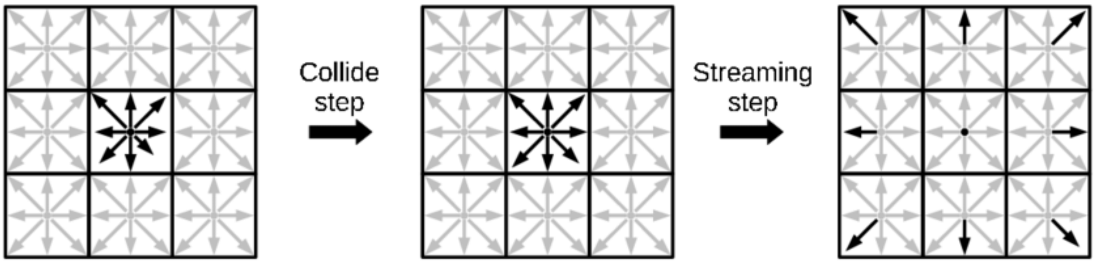

Figure 2.2: Time evolution in LB [28]. In the collision step the distributions are relaxed by the collision operator. In the streaming step, also known as propagation, the distributions propagate to the adjacent lattice point in their specific direction. These two steps alternate in the LB algorithm.

2.2.1 Collision Scheme for Momentum

The collision operator, $\Omega(\vec{x}, t)$ is added to Equation 2.11 to complete the Lattice Boltzmann equation, see Equation 2.12.

$$f_i\left(\vec{x} + \vec{c_i}\Delta t, t + \Delta t\right) = f_i(\vec{x}, t) + \Omega_i(\vec{x}, t) \tag{2.12}$$

In this thesis the so called "Filter Matrix" method is applied to calculate the collision operator. This method was originally developed by Eggels and Somers [9]. In this section their methodology is briefly explained. In the Filter Matrix method the time formulation is staggered by $\pm\Delta t/2$ around a certain time t, see Equation 2.13.

$$f_i\left(\vec{x} + \frac{\vec{c_i}\Delta t}{2}, t + \frac{\Delta t}{2}\right) - f_i\left(\vec{x} - \frac{\vec{c_i}\Delta t}{2}, t - \frac{\Delta t}{2}\right) = \mathbf{\Omega}_i(\vec{x}, t) \tag{2.13}$$

From the pre-collision distribution a vector α_k^- is calculated by means of a matrix multiplication with the matrix E_{ki} in Equation 2.14. The vector α_k^- represents a set of physical parameters of the pre-collision distribution.

$$\alpha_k^- = \sum_i \boldsymbol{E}_{ki} f_i \left(\vec{x} - \frac{\vec{c}_i \Delta t}{2}, t - \frac{\Delta t}{2} \right) \tag{2.14}$$

Here the matrix $\boldsymbol{E}_{ki}$ is given by Equation 2.15 [52]:

$$\begin{aligned} \boldsymbol{E}_{ki} = \big[& 1, c_{ix}, c_{iy}, 3c_{ix}^2 - 1, 3c_{ix}c_{iy}, 3c_{iy}^2 - 1, \\ & c_{ix}\left(3c_{iy}^2 - 1\right), c_{iy}\left(3c_{ix}^2 - 1\right), \frac{\left(3c_{ix}^2 - 1\right)\left(3c_{iy}^2 - 1\right)}{2} \ ]. \end{aligned} \tag{2.15}$$

And α_k^- specifies the vector given in Equation 2.16 [52]:

$$\alpha_k^-(\vec{x}, t) = \begin{bmatrix} \rho \\ \rho u_x - \frac{\Delta t}{2} F_x \\ \rho u_y - \frac{\Delta t}{2} F_y \\ 3\rho u_x u_x + \rho\left(-6\nu - \Delta t\right) \frac{\partial u_x}{\partial x} \\ 3\rho u_x u_y + \frac{\rho(-6\nu - \Delta t)}{2} \left(\frac{\partial u_x}{\partial y} + \frac{\partial u_y}{\partial x} \right) \\ 3\rho u_y u_y + \rho\left(-6\nu - \Delta t\right) \frac{\partial u_y}{\partial y} \\ T_1^- \\ T_2^- \\ F_1^- \end{bmatrix} \tag{2.16}$$

Here F_x and F_y represent the x and y components of the applied body force. In similar fashion u_x and u_y represent the x and y components of the velocity. Lastly, $T_1^{\pm}$, $T_2^{\pm}$ and $F_1^{\pm}$ represent higher order terms. For the simulations of thermal convective flow the Boussinesq approximation is used. Equation 2.17 gives the force generated by the thermal buoyancy effect:

$$\vec{F} = -\rho_0 \vec{g}_{grav} \beta_{exp} (T - T_0), \tag{2.17}$$

where ρ_0 is the average density of the fluid, $\vec{g}_{grav}$ is the gravitational acceleration, β_{exp} is the thermal expansion coefficient and T_0 is the mean of the coldest and the hottest part of the fluid. In the case of a melting problem the coldest temperature is the melting point of the fluid.

Given that α_k^- is known, a new vector α_k^+, as defined in Equation 2.18, can be calculated which can be transformed back into the post-collision distribution. This is given in Equation 2.19.

$$\alpha_k^+(\vec{x},t) = \begin{bmatrix} \rho \\ \rho u_x + \frac{\Delta t}{2} F_x \\ \rho u_y + \frac{\Delta t}{2} F_y \\ 3\rho u_x u_x + \rho\left(-6\nu + \Delta t\right) \frac{\partial u_x}{\partial x} \\ 3\rho u_x u_y + \frac{\rho(-6\nu+\Delta t)}{2} \left(\frac{\partial u_x}{\partial y} + \frac{\partial u_y}{\partial x}\right) \\ 3\rho u_y u_y + \rho\left(-6\nu + \Delta t\right) \frac{\partial u_y}{\partial y} \\ T_1^+ \\ T_2^+ \\ F_1^+ \end{bmatrix} \tag{2.18}$$

$$f_i\left(\vec{x} + \frac{\vec{c}_i \Delta t}{2}, t + \frac{\Delta t}{2}\right) = \sum_k \omega_i \boldsymbol{E}_{ik} \alpha_k^+, \tag{2.19}$$

where ω_i represent the weights that are associated with the distributions in Lattice Boltzmann scheme. In this D2Q9 scheme the weights are given by Equation 2.20:

$$\omega_i = \begin{cases} 4/9 & i = 0 \\ 1/9 & i = 1, 2, 3, 4 \\ 1/36 & i = 5, 6, 7, 8 \end{cases} \tag{2.20}$$

and the matrix $\boldsymbol{E}_{ik}$ is given by Equation 2.21 [52]:

$$\begin{aligned} \boldsymbol{E}_{ik} = \Bigg[& 1, 3c_{ix}, 3c_{iy}, \frac{3c_{ix}^2 - 1}{2}, 3c_{ix}c_{iy}, \frac{3c_{iy}^2 - 1}{2}, \frac{3c_{ix}\left(3c_{iy}^2 - 1\right)}{2}, \\ & \frac{3c_{iy}\left(3c_{ix}^2 - 1\right)}{2}, \frac{\left(3c_{ix}^2 - 1\right)\left(3c_{iy}^2 - 1\right)}{2} \Bigg]. \end{aligned} \tag{2.21}$$

In order to apply the momentum part of the FMLB scheme one needs to provide a solution for Equation 2.19. This is done by using the following solution for α_k^+, as in Equation 2.22:

$$\alpha_k^+ = \begin{bmatrix} \rho \\ \alpha_1^- + \Delta t F_x \\ \alpha_2^- + \Delta t F_y \\ G(\alpha_3^- - 3\rho u_x^2) + 3\rho u_x^2 \\ G(\alpha_4^- - 3\rho u_x u_y) + 3\rho u_x u_y \\ G(\alpha_5^- - 3\rho u_y^2) + 3\rho u_y^2 \\ -\gamma_1 \alpha_6^- \\ -\gamma_1 \alpha_7^- \\ -\gamma_2 \alpha_8^- \end{bmatrix}. \tag{2.22}$$

The velocity and density can be obtained from α_k^-, see Equation 2.23 and 2.24:

$$\vec{u} = \begin{bmatrix} (\alpha_1^- + \Delta t F_x)/\rho_0 \\ (\alpha_2^- + \Delta t F_y)/\rho_0 \end{bmatrix} \tag{2.23}$$

$$\rho = \alpha_0^- \tag{2.24}$$

The constant G is given by Equation 2.25:

$$G = \frac{-6\nu + 1}{-6\nu - 1} \tag{2.25}$$

To reckon with the influence of the melting front on the impulse scheme the enthalpy porosity method is implemented [23]. Equation 2.12 is adjusted in the following manner, as shown in Equation 2.26:

$$f_i\left(\vec{x} + \vec{c}_i\Delta t, t + \Delta t\right) = f_i(\vec{x}, t) + (1 - B)\Omega_i(\vec{x}, t) + B(f_{\bar{i}}(\vec{x}, t) - f_i(\vec{x}, t)), \tag{2.26}$$

where

$$B = \frac{(1 - f_L)\nu/c^2}{f_L + \nu/c^2} \tag{2.27}$$

gives a measure of the porosity of the liquid. Here $B = 0$ equates to purely fluid and and $B = 1$ to purely solid, anywhere in between is the mushy zone. In this equation the first term is just the pre-collision distribution. The second term is the collision operator scaled by $(1 - B)$ which accounts for the porosity. The third term specifies a bounce-back of momentum on the potential phase-change interface. The index $\bar{i}$ represents the opposite direction of index i.

2.2.2 Collision Scheme for Heat

For the transport of heat another Lattice Boltzmann scheme is used with the distributions labeled as $g_i(\vec{x}, t)$. The sum of these distributions form the total enthalpy in a specific point $\vec{x}$ at time t, as shown in Equation 2.28

$$H(\vec{x}, t) = \sum_i g_i(\vec{x}, t) \tag{2.28}$$

This distribution is applied in the Lattice Boltzmann equation, given in 2.29:

$$g_i\left(\vec{x} + \vec{c}_i\Delta t, t + \Delta t\right) = g_i(\vec{x}, t) + \Psi_i(\vec{x}, t), \tag{2.29}$$

where $\Psi(\vec{x}, t)$ denotes the collision operator on the thermal distribution.

The enthalpy consists of two parts, which is shown in Equation 2.30:

$$H = C_p T + f_L L. \tag{2.30}$$

Here C_p, f_L and L refer to the heat capacity, fluid fraction and latent heat of melting. The fluid fraction is a value between 0 and 1, where 0 means solid, 1 means fluid and anywhere in between is considered to be the "mushy zone". In Equation 2.30 C_pT is referred to as the sensible heat, henceforward denoted with the superscript "s", and f_LL is the latent, denoted with the superscript "l".

From Equation 2.30 and inverse relation can be distilled for the temperature and fluid fraction, see Equations 2.31 and 2.32 [18]:

$$T = \begin{cases} H/C_p & H < H_s \\ T_s + \frac{H-H_s}{H_l-H_s}\left(T_l - T_s\right) & H_s \leq H \leq H_l \\ T_l + \left(H - H_l\right)/C_p & H > H_l \end{cases}, \tag{2.31}$$

$$f_L = \begin{cases} 0 & H < H_s \\ \frac{H-H_s}{H_l-H_s} & H_s \leq H \leq H_l \\ 1 & H > H_l \end{cases}, \tag{2.32}$$

where T_s and T_l are the solidus and liquidus temperatures, the difference between these is the width of the mushy zone, ϵ. H_l is the solidus enthalpy, defined as C_pT_s and H_s the liquidus enthalpy, defined as $H_s + L$.

The enthalpy distribution is split into a sensible part and a latent heat part as defined by equations 2.33 and 2.34. Here the latent heat is considered to be part of the stationary distribution by the assumption that the latent heat does not diffuse since it does not contribute to a temperature difference. If, for instance, a solid with a certain temperature T is adjacent to a fluid with identical temperature the net heat transfer through the sold-liquid interface would be zero as heat can only diffuse from a warmer to a colder body on the macroscopic scale [43].

$$g_i(\vec{x}, t) = g_i^s(\vec{x}, t) + g_i^l(\vec{x}, t) \tag{2.33}$$

$$g_i^l(\vec{x}, t) = \left[f_L L, 0, 0, 0, 0, 0, 0, 0, 0\right]^T \tag{2.34}$$

The collision operation on the thermal distribution is therefore only applied on the sensible part of the heat, see Equation 2.35:

$$g_i^s\left(\vec{x} + \frac{\vec{c}_i \Delta t}{2}, t + \frac{\Delta t}{2}\right) - g_i^s\left(\vec{x} - \frac{\vec{c}_i \Delta t}{2}, t - \frac{\Delta t}{2}\right) = \mathbf{\Psi}_i(\vec{x}, t). \tag{2.35}$$

Splitting the total enthalpy into a sensible part and latent heat part allows us to perform calculations without the use of computationally expensive iterative schemes such the linearized enthalpy mehtod [40, 11]. This method of splitting the total enthalpy was inpsired by Huang et al. [18]. Another possibility is to define the rate of change in the fluid fraction in terms g_i and solve Equation 2.7 [10]. This, however, requires to solve a system of equations, requiring a lot of computational expense.

In a likewise procedure with respect to the collision scheme for momentum the pre-collision distribution is transformed into a vector of physical parameters, β_k^-, by means of Equation 2.36:

$$\beta_k^- = \sum_i \boldsymbol{E}_{ki} g_i^s \left(\vec{x} - \frac{\vec{c}_i \Delta t}{2}, t - \frac{\Delta t}{2} \right), \tag{2.36}$$

where $\beta_k^\pm$ is defined by Equation 2.37 [52]:

$$\begin{aligned} \beta_k^\pm(\vec{x}, t) = \Bigg[& T, u_x T + \frac{-6\alpha \pm \Delta t}{6} \frac{\partial T}{\partial x}, u_y T \\ & + \frac{-6\alpha \pm \delta t}{6} \frac{\partial T}{\partial y}, S_1^\pm, S_2^\pm, S_3^\pm, T_1^\pm, T_2^\pm, F^\pm \Bigg]^{\mathrm{T}}. \end{aligned} \tag{2.37}$$

From β_k^+ the post-collision distribution is found by a reverse transformation of Equation 2.36 given by Equation 2.38:

$$g_i^s \left(\vec{x} + \frac{\vec{c}_i \Delta t}{2}, t + \frac{\Delta t}{2} \right) = \sum_k \omega_i \boldsymbol{E}_{ik} \beta_k^+. \tag{2.38}$$

As a sidenote: After the collision step is performed the total enthalpy in a node remains unchanged, likewise the amount of heat in the stationary distribution also remains unchanged after the collision step, which means that the latent heat remains unchanged. In fact, the total enthalpy is only changed by the propagation step as the sum of the distributions changes. From this new total enthalpy a new temperature and fluid fraction are calculated which defines the separation between sensible and latent heat.

Similar to solving Equation 2.19 for the impulse scheme we solve Equation 2.38 for the thermal scheme. The solution for β_k^+ is given by Equation 2.39:

$$\beta_k^+ = \begin{bmatrix} T \\ \bar{G}(\beta_1^- - Tu_x) + Tu_x \\ \bar{G}(\beta_2^- - Tu_y) + Tu_y \\ -\gamma_2\alpha_3^- \\ -\gamma_2\alpha_4^- \\ -\gamma_2\alpha_5^- \\ 0 \\ 0 \\ 0 \end{bmatrix}. \tag{2.39}$$

Where T is given by β_0^- and $\vec{u}$ is extracted from the impulse scheme. Similar to the impulse scheme, $\bar{G}$ is given by Equation 2.40:

$$\bar{G} = \frac{-6\alpha + 1}{-6\alpha - 1} \tag{2.40}$$

3 Methodology

In this section the implementation of boundary conditions is explained. In addition is the implementation of Adaptive Mesh Refinement given with the applied criteria for refinement. At last, are the benchmarks given used to validate the code. A general overview of all these operations can be found in Appendix 6.0.1

3.1 Boundary conditions

For the density distribution the half-way bounce back boundary conditions are used. This means that the boundary is the perimeter of a distance of $\Delta x/2$ around the lattice points. As shown in Figure [45] the distributions are reflected in opposite direction. This forces the velocity along the wall to be zero; it enforces a 'stick boundary' [45].

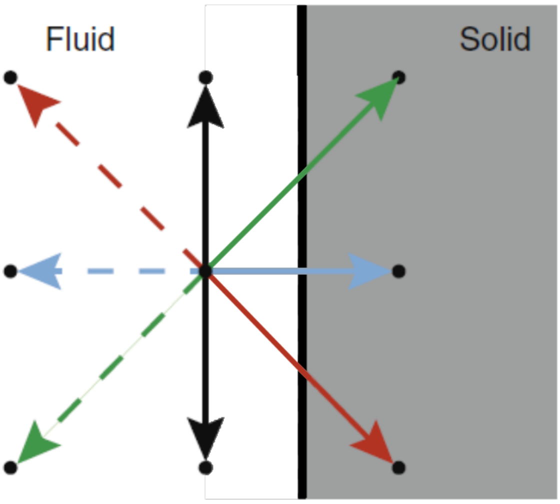

Figure 3.1: Schematic of the half-way bounce-back condition. The distributions are reflected to the inverse direction on the imaginary wall which represents the boundary of the domain [1].

Two types of boundary conditions are applied to the temperature scheme: the isothermal (Dirichlet) and zero-flux boundary conditions. For the isothermal boundary condition, the bounce-back method is applied (Equation 3.2) in the propagation step to enforce the wall temperature, T_w [50]:

$$g_i\left(\vec{x}+\vec{c}_i\Delta t, t+\Delta t\right) = 2\omega_{\bar{i}}T_w - (g_{\bar{i}}(\vec{x},t) + \Psi(\vec{x},t)). \tag{3.1}$$

As such Equation 3.2 replaces Equation 2.29 for the concerning boundary nodes, for the directions, i, moving out of the boundary. Hence, if $\hat{n}$ is the normal to the boundary going inwards to the geometry, it concerns those directions for which $\hat{n} \cdot \vec{c}_i > 0$. The zero-flux boundary is formulated by defining the wall temperature as the temperature of the node adjacent to the wall. For instance if the zero-flux boundary is applied to $y = 0$ the definition becomes [50]:

$$g_i \left(\begin{bmatrix} x \\ 0 \end{bmatrix} + \vec{c}_i \Delta t, t + \Delta t \right) = 2\omega_{\bar{i}} T \begin{bmatrix} x \\ 1 \end{bmatrix} - \left(g_{\bar{i}} \left(\begin{bmatrix} x \\ 0 \end{bmatrix}, t \right) + \Psi \left(\begin{bmatrix} x \\ 0 \end{bmatrix}, t \right) \right), \tag{3.2}$$

again for those directions that satisfy $\hat{n} \cdot \vec{c}_i > 0$, i.e. the directions going into the domain.

3.2 Adaptive Mesh Refinement

Using adaptive mesh refinement, certain parts of the domain can calculated on a fine grid, whilst other cells can remain coarse. Taking into consideration that the collision operator requires two matrix-vector multiplications, this step compromises the majority of the computational expense.

3.2.1 Collision and Propagation

The implementation of mesh refinement is based on earlier work by Rohde et al. [34], yet in a simplified manner; such that only the collision operation is performed on either the coarse grid or the fine grid, depending if a cell is refined or not but the propagation is always on the finest grid. In the method by Rohde et al [34] the propagation on the coarse cells is performed on a coarse grid and the cells that lay in between the coarse and fine grid are temporarily refined in order to communicate changes on the fine grid to the coarse grid. Numerically this gives the exact same results for possibly shorter calculation times, yet requiring a lot more coding. Here we will discuss the methodology for one refinement level, for the simplified scheme where propagation happens on the finest grid.

Initially a cell is identified that needs to be refined under some arbitrary criterion. In Figure 3.2a this cell is marked in green. The cell is first split into four smaller cells which have the exact same distributions, i.e. densities, as the larger parent cell, see Figure 3.2b. Then the collision is performed only on the cells in the fine grid as shown in Figure 3.2c. In succession, these changes need to be communicated to the surrounding grid. In order to do so, the coarse cells are temporarily split into finer cells. This is again done by splitting the coarse cells into smaller cells with equal distributions as shown Figure 3.2d, likewise the process described in Figure 3.2b.

Then the propagation step is performed on the fine grid as seen in Figure 3.2e. After the post-collision distributions of the fine grid have been communicated to the cells belonging to the coarse grid, these cells can be made coarse again. This is done by averaging the distributions of the four child cells, as seen in Figure 3.2f.

Subsequently these steps are repeated but now the collision is performed on both the fine and coarse grid. Figure 3.2g shows the collision on both grids, then again the coarse cells are split, see Figure 3.2h. After which the propagation is performed, as shown in Figure 3.2i and after that the temporarily split cells are once again averaged to become the coarse grid again, the result of which is shown in Figure 3.2j. This completes one time step.

Notice that collision is performed once on the coarse grid and twice on the fine grid for each time step, hence potentially reducing the calculation time significantly. In addition, the propagation step is performed twice on the fine grid.

3.2.2 Computational Time Reduction

The computational expense grows rather fast with increasing fineness. In fact, the expense grows by a power of 4 with respect to the refinement. This is because the number of gridpoints grows quadratically if a coarse grid is replaced by a fine grid and, under the condition that the value of the thermal diffusivity and heat conductivity in LB units ($\Delta x^2/\Delta t$) are left unchanged, the size of the time step has to be decreased quadratically.
The case for adaptive grid refinement is made by the logic that one might only need a fine grid on certain parts of the domain. The savings in computational expense stem from the fact the collision operator doesn't need to be calculated on the entire fine grid, which has 4 cells for 1 coarse cells and requires the collision to be performed twice on each of these 4 child cells. Which means that a fine cell needs 8 collision operations in one time step instead of one for coarse cell. The collision operation is costly since it requires two matrix-vector multiplications with 9×9 matrices.

However the adaptive grid refinement also brings in some computational expense. In this implementation the propagation step is performed on the fine grid which makes this more expensive and also twice as frequent for the coarse cells. The expense of the propagation step is however very minor compared to the propagation step, since it only requires moving elements in an array. Besides that, does it require to split the coarse cells before the propagation step and average them again after the propagation. Lastly, is there overhead from checking refinement criteria.

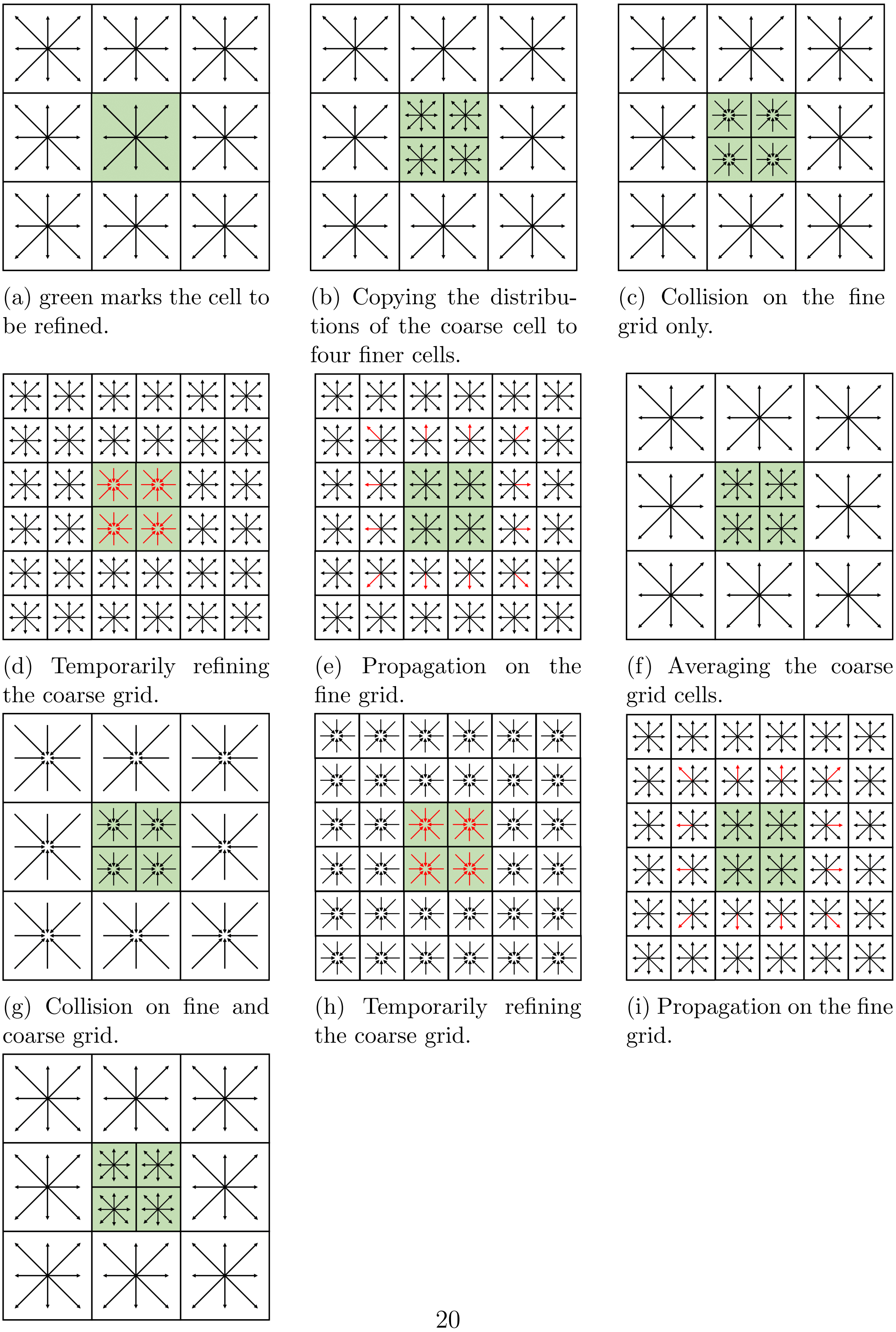

(a) green marks the cell to be refined.

(b) Copying the distributions of the coarse cell to four finer cells.

(c) Collision on the fine grid only.

(d) Temporarily refining the coarse grid.

(e) Propagation on the fine grid.

(f) Averaging the coarse grid cells.

(g) Collision on fine and coarse grid.

(h) Temporarily refining the coarse grid.

(i) Propagation on the fine grid.

(j) Averaging the coarse grid cells

Figure 3.2: Figures a through j give the steps of the adaptive mesh refinement method.

3.2.3 Re-scaling of variables

The magnitude of the cells is halved for each refinement, see Equation 3.3.

$$\Delta x_n = \Delta x \cdot 2^{-n}, \tag{3.3}$$

where n is the level of refinement, Δx is the magnitude of the cell size on the coarsest grid and the subscript n in Δx_n indicates the value of that variable in the n^{th} refinement. A value of $n = 0$ represents the coarse grid, $n = 1$ the first refinement etc. The size of the time step is scaled scaled by Equation 3.4 in order to keep the lattice speed fixed in the refined cells.

$$\Delta t_n = \Delta t \cdot 2^{-n} \tag{3.4}$$

As both *alpha* and *nu* have units of m^2/s they are scaled by the following relations, see Equations 3.5, 3.6

$$\alpha_n = \alpha \cdot 2^{-n} \tag{3.5}$$

$$\nu_n = \nu \cdot 2^{-n} \tag{3.6}$$

These rescaled values for the thermal diffusivity and viscosity are used to rescale G and $\bar{G}$, as shown in Equations 3.7 and 3.8:

$$G_n = \frac{-6\nu_n + 1}{-6\nu_n - 1} \tag{3.7}$$

$$\bar{G}_n = \frac{-6\alpha_n + 1}{-6\alpha_n - 1}. \tag{3.8}$$

The body force is in LB units is scaled by Equation 3.9:

$$\vec{F}_n = \vec{F} \cdot 2^n. \tag{3.9}$$

Which is used for the calculations of the velocity, see Equation 2.23, the value on a refined grid n is found through Equation 3.10:

$$\vec{u}_n = \begin{bmatrix} (\alpha^-_{1,n} + \Delta t_n F_{x,n})/\rho_0 \\ (\alpha^-_{2,n} + \Delta t_n F_{y,n})/\rho_0 \end{bmatrix} \tag{3.10}$$

Where $\alpha^-_{k,n}$ marks the value of α^-_i on refinement level n and is just found by Equation 2.14. The value of α^+_k on the refined grid, $\alpha^+_{k,n}$, is obtained through 2.22 by adjusting the values to the appropriate refinement, as in Equation 3.11:

$$\alpha^{+}_{k,n} = \begin{bmatrix} \rho \\ \alpha^{-}_{1,n} + \Delta t_n F_{x,n} \\ \alpha^{-}_{2,n} + \Delta t_n F_{y,n} \\ G(\alpha^{-}_{3,n} - 3\rho u^2_{x,n}) + 3\rho u^2_{x,n} \\ G(\alpha^{-}_{4,n} - 3\rho u_{x,n} u_{y,n}) + 3\rho u_{x,n} u_{y,n} \\ G(\alpha^{-}_{5,n} - 3\rho u^2_{y,n}) + 3\rho u^2_{y,n} \\ -\gamma_1 \alpha^{-}_{6,n} \\ -\gamma_1 \alpha^{-}_{7,n} \\ -\gamma_2 \alpha^{-}_{8,n} \end{bmatrix}. \tag{3.11}$$

β^{+}_{k} can be found on the refined grid in a similar fashion by implementing $\bar{G}_n$ and $\vec{u}_n$ in Equation 2.39, see Equation 3.12:

$$\beta^{+}_{k,n} = \begin{bmatrix} T \\ \bar{G}_n(\beta^{-}_{1,n} - Tu_{x,n}) + Tu_{x,n} \\ \bar{G}_n(\beta^{-}_{2,n} - Tu_{y,n}) + Tu_{y,n} \\ -\gamma_2 \alpha^{-}_{3,n} \\ -\gamma_2 \alpha^{-}_{4,n} \\ -\gamma_2 \alpha^{-}_{5,n} \\ 0 \\ 0 \\ 0 \end{bmatrix}. \tag{3.12}$$

3.3 Benchmark Cases

Benchmarks are used to validate the methodology. The Stefan Problem is used to validate the implementation of the latent heat source term in the thermal FMLB scheme. In addition, do we apply grid refinement to the Stefan Problem set against a case without refinement to compare computational time.

3.3.1 Stefan Problem

In the Stefan Problem, 1-dimensional melting is simulated and compared to an analytical solution. In Figure 3.3 a representation is given of this geometry. Here the left side is an isothermal hot wall at temperature T_H and the right side an isothermal cold wall at temperature T_C. The upper and lower boundary have a zero net flux perpendicular to the bounds. The red on the left side marks the fluid and the blue on the right marks the solid material. This interface is moving to the right upon melting. The variables that have been used for this problem are given in Table 1.

Table 1: Parameters used for the Stefan problem for no refinement

Variable	**Physical Meaning**	**value, unit**
L_x	Size in the x-direction	1.28 cm
L_y	Size in the y-direction	0.32 cm
N_x	Number of cells in the x-direction	64
N_y	Number of cells in the y-direction	16
Δx	Magnitude of coarsest cell	0.02 cm
Δt	Magnitude of time step	$5.628 \cdot 10^{-4}$ s
α_{phys}	Physical value of the thermal diffusivity	$1.422 \cdot 10^{-5}$ m^2/s
α	Thermal diffuvisity in LB units	$0.2\Delta x^2/\Delta t$
L	Latent heat	80160 J
C_p	Heat capacity	381 J/(kg K)
Ste	Stefan number	0.0941
k	solution to the transcendental equation	0.2133
T_H	Hot wall temperature	320.93 K
T_C	Cold wall temperature	300.93 K
T_m	Melting point	301.13 K
T_0	Initial temperature	300.93 K
ϵ	Width of the mushy zone	0.2 K

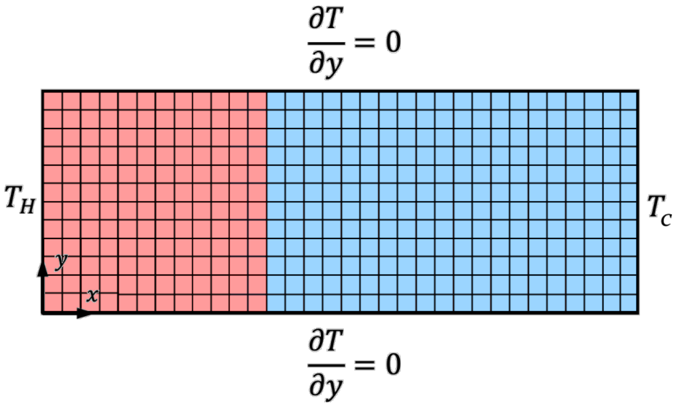
$\frac{\partial T}{\partial y} = 0$
T_H
T_c
y
x
$\frac{\partial T}{\partial y} = 0$

Figure 3.3: Representation of the Stefan Problem for no refinement.

Besides the case where the entire mesh is fine, two other cases are investigated with 1 and 2 levels of refinement. The method of refinement is explained in the following two paragraphs. The representations of the resulting meshes are given in Figures 3.7 and 3.11.

One level of Refinement

For a single refinement the refined cells are defined as such that in the initial condition the leftmost two layers of coarse cells of the geometry are refined. For tracking the melting interface the fluid fraction, f_L, is projected on the fine grid by splitting the coarse grid cells into 4 smaller cells. Upon melting the solid nodes are identified by where $f_L < 0.5$ on the fine grid. The inner boundary of this solid domain, excluding the bounds the geometry; i.e. the leftmost fine cells of the solid domain, are identified as a part of the phase change region, see Figure 3.4. In addition, the neighbours to the solid nodes; i.e. the right most cells of the fluid domain on the fine grid, are identified as a part of the phase change region 3.4.

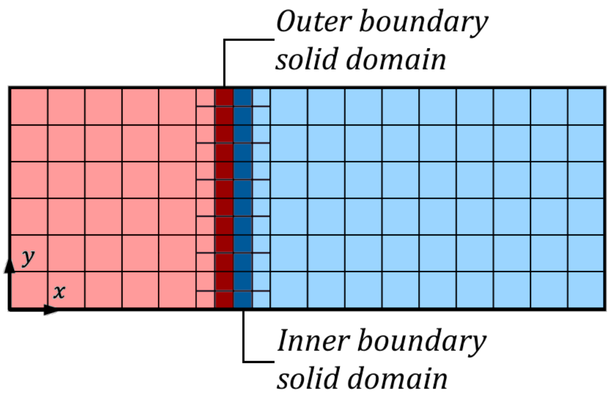

Figure 3.4: Representation of the Stefan Problem for one level of refinement. The dark blue cells show the inner boundary of the solid domain and the darker red cells mark the outer boundary of the solid domain. The union of these is the phase change region.

For this phase change region the parent cells are found on the coarse grid and are refined, see Figure 3.5.

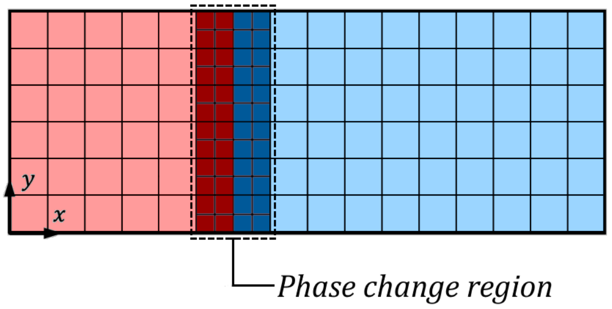

Figure 3.5: Representation of the Stefan Problem for one level of refinement. The parent cells of the phase region are identified and refined.

If the phase change interface moves one fine grid cell to the right it is still on the fine grid. If it then moves an additional fine grid cell to the right the phase change region is between a fine and a coarse grid cell. However, since the inner boundary of the solid domain is refined, the bordering coarse cells will become fine and a such the phase change region is always on the fine grid, see Figure 3.6

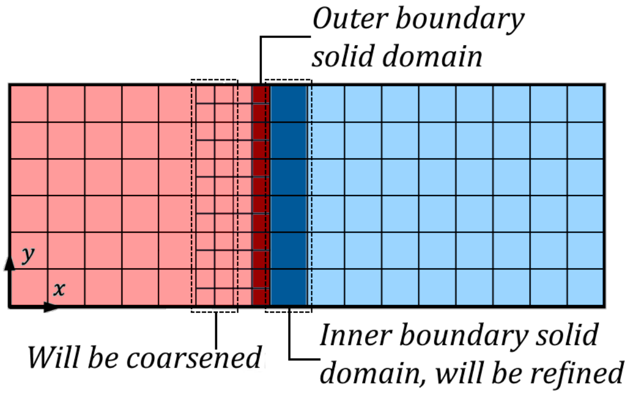
Outer boundary solid domain
y
x
Will be coarsened
Inner boundary solid domain, will be refined

Figure 3.6: Representation of the Stefan Problem for one level of refinement. The phase change region is between the fine and the coarse grid. The coarse grid cells at the phase change region belong to the inner boundary of the solid domain and are that reason refined. The cells on the left of the phase change region no longer contain the phase charge interface and are for that reason coarsened.

A final representation of this grid is shown in Figure 3.7. Notice that the solid-liquid interface has moved to the right.

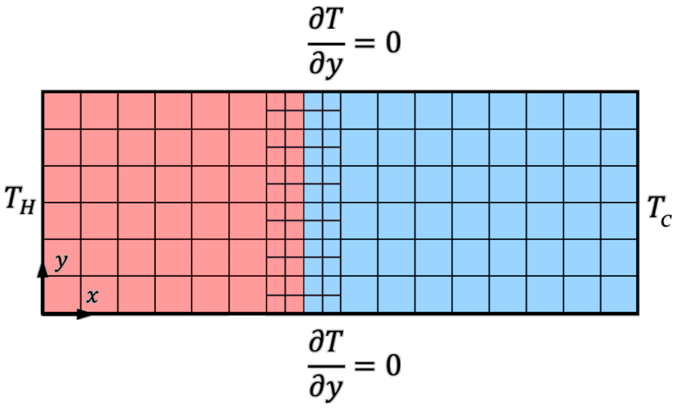
$\frac{\partial T}{\partial y} = 0$
T_H
T_c
y
x
$\frac{\partial T}{\partial y} = 0$

Figure 3.7: Representation of the Stefan Problem for one level of refinement.

The variables on the coarse cells are the same as in Table 1, apart from Δx and

Δt which are 0.04 cm and $2.251 \cdot 10^{-3}$ s for the coarse cells. The values on the refined cells are scaled as explained in Section 3.2.3.

Two levels of Refinement

For two levels of refinement a quite similar procedure is followed. The paramter n defines the fineness of the grid, where $n = 2$ is the finest cell and $n = 0$ the coarsest. The fluid fracton is projected on the finest, $n = 2$, grid on which phase change region is defined, see Figure 3.8.

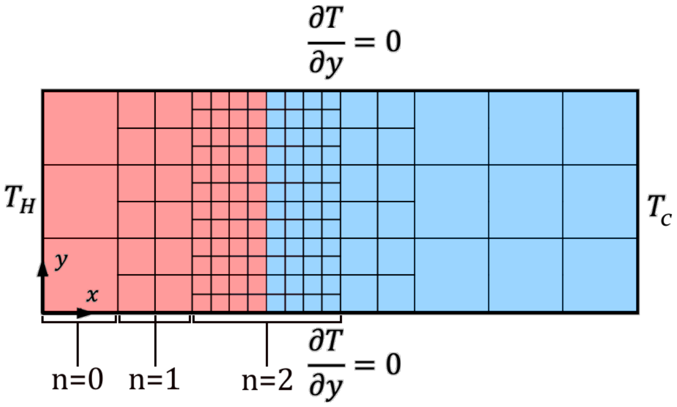
$\frac{\partial T}{\partial y} = 0$
T_H
T_c
y
x
n=0
n=1
n=2
$\frac{\partial T}{\partial y} = 0$

Figure 3.8: Representation of the Stefan Problem for two levels of refinement. The figure shows the size of the cells for different levels of refinement, n.

Again is the phase change region defined as the union of the inner boundary of the solid domain and the neighbours to this solid domain, see Figure 3.9.

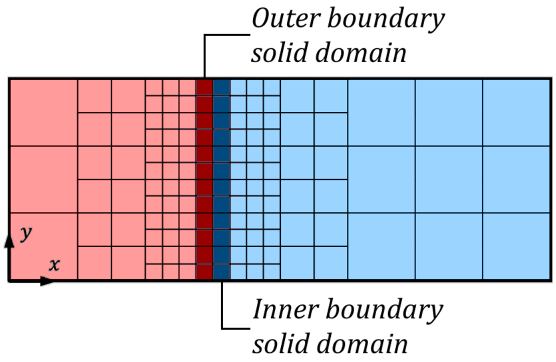

Figure 3.9: Representation of the Stefan Problem for two levels of refinement. The dark blue cells show the inner boundary of the solid domain and the darker red cells mark the outer boundary of the solid domain. The union of these is the phase change region.

Of this phase change region the cells are found in the coarsest grid, $n = 0$, of which they are a part of. These coarse grid cells are kept at a refinement of $n = 2$, the finest grid, see Figure 3.10.

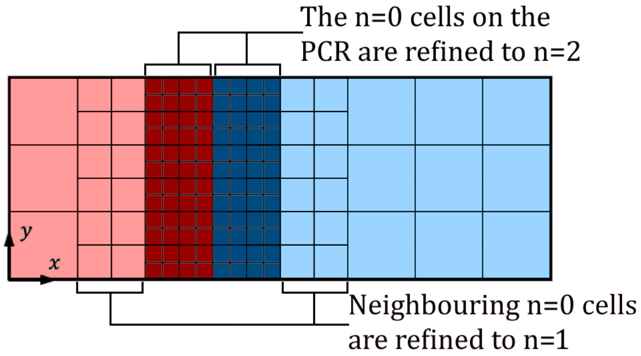
The n=0 cells on the PCR are refined to n=2
y
x
Neighbouring n=0 cells are refined to n=1

Figure 3.10: Representation of the Stefan Problem for one level of refinement. The $n = 0$ cells on which the phase region lies are identified and refined.

The cells bordering these coarse grid cells, are refined to $n = 1$, see Figure 3.10. When the phase change region moves to the right it will remain on the $n = 2$ grid until it borders the $n = 1$ grid. Correspondingly to one level of refinement, upon bordering the $n = 1$ grid by the phase change region on the right side, these $n = 1$ cells are refined to $n = 2$ since the inner boundary of the solid domain is refined to the finest $n = 2$ grid. As such the phase change region remains on the finest grid. A final representation of the grid, after moving of the interface, is shown in Figure 3.11

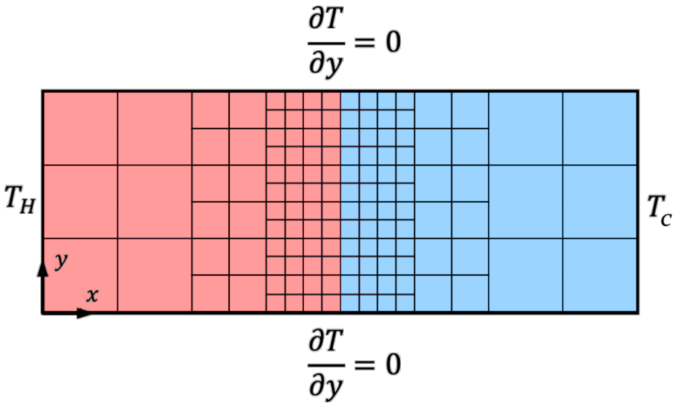
$\frac{\partial T}{\partial y} = 0$
T_H
T_c
y
x
$\frac{\partial T}{\partial y} = 0$

Figure 3.11: Representation of the Stefan Problem for two levels of refinement.

The variables on the coarse grid cells for this case are again the same as for no refinement, see Table 1, apart from Δx and Δt which are 0.08 cm and $9.004 \cdot 10^{-3}$ s for the coarsest cells.

Analytical Solution to the Stefan Problem
In the Stefan Problem a comparison is made to an analytical solution. This solution is defined by the transcendental equation. The melting front, x_{pc}, moves forward by the relation:

$$x_{pc} = 2k\sqrt{\alpha t}. \tag{3.13}$$

Where k is the solution of the transcendental equation, Equation 3.14 [47]:

$$\frac{e^{-k^2}}{k\,\mathrm{erf}(k)} = Ste\sqrt{\pi}, \tag{3.14}$$

Where Ste is the Stefan number which is a non-dimensional ratio between sensible and latent heat characterized by the hot wall temperature, T_H; melting point, T_m and latent heat, L, see Equation 3.15:

$$Ste = \frac{C_p(T_H - T_m)}{L} \tag{3.15}$$

The temperature profile in the liquid area is then given by:

$$T = T_H - (T_H - T_m)\frac{\mathrm{erf}\left(\frac{x}{2\sqrt{\alpha t}}\right)}{\mathrm{erf}(k)} \text{ for } x < x_{pc} \tag{3.16}$$

The temperature in the solid area can be characterized by the penetration theorem initially. Note that this solution very quickly becomes inaccurate since penetration will no longer hold in case the heat reaches the right boundary.

3.3.2 Natural Convection of Air

Secondly a study has been conducted on the natural convection of air, hence implying to only be in the gaseous phase, in a square cavity and compared to a previous study [52]. In this instance refinement is based on the velocities and vorticity. The results of the adaptive mesh refinement are compared to a fully fine grid. The geometry is defined as shown in Figure 3.12. The boundary conditions are similar to the Stefan Problem.

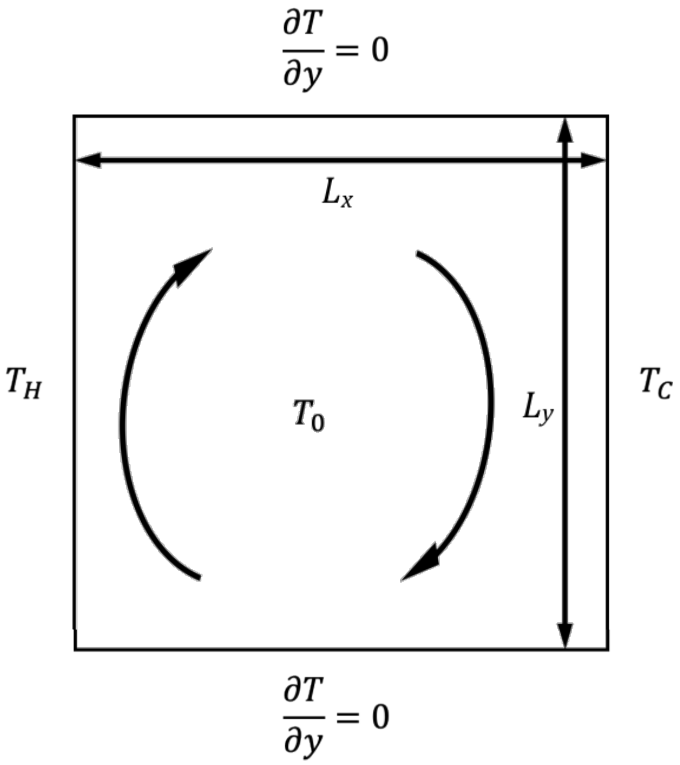
$\frac{\partial T}{\partial y} = 0$
L_x
T_H
T_0
L_y
T_C
$\frac{\partial T}{\partial y} = 0$

Figure 3.12: Representation of the geometry for natural convection in a cavity.

For this simulation the following parameters are used, see Table 2. These parameters can be reduced to three non-dimensional numbers that characterize the problem: the Rayleigh number, Ra; the Prandtl number, Pr and the Fourier number, Fo. The Rayleigh number represents the ratio between heat transport through diffusion and convection, see Equation 3.17 [21]:

$$Ra = \frac{g_{grav}\beta_{exp}(T_H - T_C)L_c^3}{\nu\alpha}, \tag{3.17}$$

where L_c is the characteristic length of the geometry. In this case $L_c = L_x = L_y$. The Prandtl number, Pr, is the ratio between the viscosity and the thermal diffusivity: $Pr = \nu/\alpha$. Lastly, the Fourier number is basically a non-dimensional representation of time as given by equation 3.18 [21]:

$$Fo = \frac{t\alpha}{L_c^2} \tag{3.18}$$

Initially a grid convergence study will be performed based upon the convergence of the minimum, maximum and average Nusselt number on the cold wall.

The Nusselt number on the cold wall is given by Equation 3.19 [52]:

$$Nu(y) = -\frac{L_y}{\Delta T}\left(\frac{\partial T}{\partial x}\right)_{x=L_x}. \tag{3.19}$$

Besides a grid convergence study the as aforementioned two cases for refinement are investigated. The first case is where areas are refined based upon the vorticity, ω, as this a is common parameter used for refinement [12, 31]. The vorticity is given by Equation 3.23:

$$\omega(i,j) = \left|\frac{\partial u_y(i,j)}{\partial x} - \frac{\partial u_x(i,j)}{\partial y}\right|. \tag{3.20}$$

If the vorticity exceeds a certain threshold, ω_{upper}, that lattice point is refined. If the vorticity in a refined cell undercuts the lower threshold, ω_{lower}, that cell is coarsened.

The gradients in ω are obtained through a finite difference on the velocity, see Equations 3.21, 3.22 and 3.23] [53]. Here i and j represent the discretized coordinates in the grid. The boundary nodes here are not considered and the vorticity is set to be 0 on the boundary nodes. This is not an issue for the refinement since the boundary cells are always refined because the bounce-back scheme is inaccurate on the coarse grid for this implementation of mesh refinement. If the boundary nodes would be coarse the boundary condition would be applied twice on the fine grid followed by a collision step on the coarse grid, this causes inaccuracies in the heat influx. Thus it is necessary to refine these nodes to the fineness of the propagation step.

$$\begin{aligned}\frac{\partial u_y(i,j)}{\partial x} \approx\, & u_y(i+1,j) - u_y(i-1,j) - \\ & \frac{1}{4}\left(u_y(i+1,j+1) - u_y(i-1,j+1) - u_y(i-1,j-1) + u_y(i+1,j-1)\right)\end{aligned} \tag{3.21}$$

$$\begin{aligned}\frac{\partial u_x(i,j)}{\partial y} \approx\, & u_x(i,j+1) - u_x(i,j-1) - \\ & \frac{1}{4}\left(u_x(i+1,j+1) + u_x(i-1,j+1) - u_x(i-1,j-1) - u_x(i+1,j-1)\right)\end{aligned} \tag{3.22}$$

$$\omega(i,j) = \left|\frac{\partial u_y(i,j)}{\partial x} - \frac{\partial u_x(i,j)}{\partial y}\right| \tag{3.23}$$

Secondly, a simulation will be performed where grid points are refined if the velocity exceeds a certain value. This is chosen because the higher order terms in the Chapman-Enskog expansion become have more impact for higher velocities [45], causing errors. Again, in this case the boundary nodes are also refined. All of these simulations are ran to converge to a steady state. The convergence is defined by minimal change in the velocity field and temperature field for any cell in the domain for an interval of 1000 time steps, see Equation 3.24 [52]:

$$\max\left\{\frac{\left|\vec{u}\left(\vec{x},t\right)-\vec{u}\left(\vec{x},t^{-}1000\Delta t\right)\right|}{\left|\vec{u}\left(\vec{x},t\right)\right|},\right.\\ \left.\sqrt{\left|\frac{T\left(\vec{x},t\right)-T\left(\vec{x},t-1000\Delta t\right)\,|}{T\left(\vec{x},t\right)}\right|}\right\}<10^{-3}. \tag{3.24}$$

Table 2: Parameters used for the simulation of natural convection of air in a cavity. The physical size of the grid is dependent on the number of mesh point since Δx is always 1 m.

Variable	**Physical Meaning**	**value, unit**
L_x	Size in the x-direction	N_x m
L_y	Size in the y-direction	N_y m
N_x	Number of cells in the x-direction	variable
N_y	Number of cells in the y-direction	variable
Δx	Magnitude of coarsest cell	1 m
Δt	Magnitude of time step	1 s
α_{phys}	Physical value of the thermal diffusivity	$2.608 \cdot 10^{-2}$ m^2/s
α	Thermal diffuvisity in LB units	$2.608 \cdot 10^{-2} \Delta x^2/\Delta t$
ν_{phys}	Physical value of the viscosity	$1.852 \cdot 10^{-2}$ m^2/s
ν	Viscosity in LB units	$1.852 \cdot 10^{-2} \Delta x^2/\Delta t$
C_p	Heat capacity	381.5 J/(kg K)
g_{grav}	Magnitude of the gravitational acceleration	9.8 m/s^2
β_{exp}	Thermal expansion coefficient	1 K^{-1}
Ra	Rayleigh number	10^5
Pr	Prandtl number	0.71
T_H	Hot wall temperature	19°C
T_C	Cold wall temperature	1°C
T_0	Initial temperature	10.5°C

3.3.3 Cavity Melting of Gallium

Finally, a simulation for melting in a rectangular cavity is performed, see Figure 3.13. This combines the two earlier cases for the melting in the Stefan Problem and the natural convection in the air convection case. Firstly a grid convergence study is done after which the converged grid is chosen to be the fine grid. In the adaptive mesh refinement simulations the size of the refined cells are equal to the cell size of this converged grid.

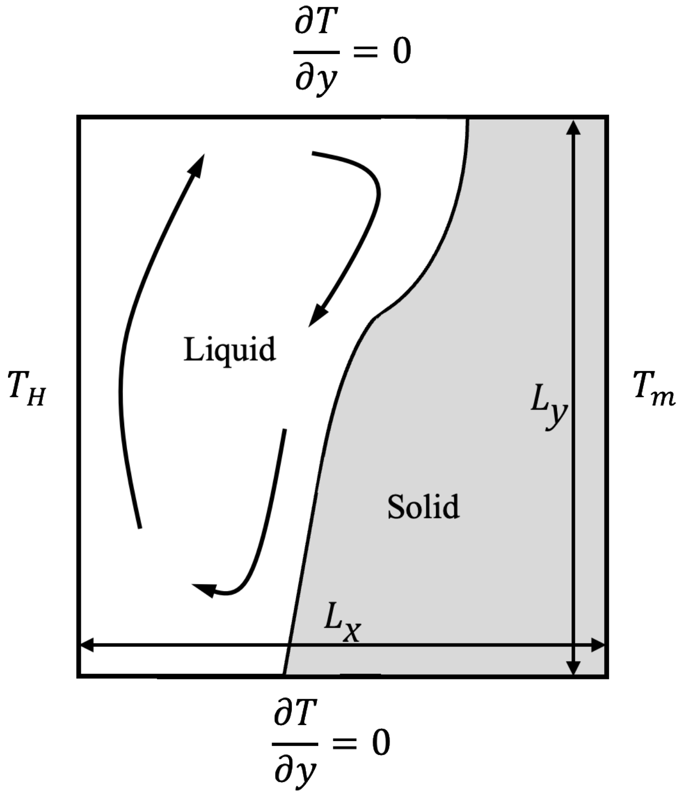

$\frac{\partial T}{\partial y} = 0$
Liquid
T_H
L_y
T_m
Solid
L_x
$\frac{\partial T}{\partial y} = 0$

Figure 3.13: Representation of cavity melting. The curved arrows represent the flow of the liquid.

Refinement is applied to the boundaries and the phase change region, in similar fashion as the Stefan problem. In addition to these two, another criterion is added: either the absolute velocity, absolute vorticity or the shear rate. The shear rate, $\dot{\gamma}$, is given by Equation 3.25 and is represented by the determinant of the shear rate tensor. The gradients in this tensor can be found from the collision step, see Equations 3.26, 3.27 and 3.28.

$$\dot{\gamma} = \sqrt{det\left(\begin{bmatrix} 2\frac{\partial u_x}{\partial x} & \frac{\partial u_x}{\partial y} + \frac{\partial u_y}{\partial x} \\ \frac{\partial u_x}{\partial y} + \frac{\partial u_y}{\partial x} & 2\frac{\partial u_y}{\partial y} \end{bmatrix}\right)} = \sqrt{4\frac{\partial u_x}{\partial x}\frac{\partial u_y}{\partial y} - \left(\frac{\partial u_x}{\partial y} + \frac{\partial u_y}{\partial x}\right)^2} \tag{3.25}$$

$$\frac{\partial u_x}{\partial x} = \frac{1}{2\Delta t}(\alpha_3^+ - \alpha_3^-) \tag{3.26}$$

$$\frac{\partial u_y}{\partial y} = \frac{1}{2\Delta t}(\alpha_5^+ - \alpha_5^-) \tag{3.27}$$

$$\frac{1}{2}\left(\frac{\partial u_x}{\partial y} + \frac{\partial u_y}{\partial x}\right) = \frac{1}{2\Delta t}(\alpha_4^+ - \alpha_4^-) \tag{3.28}$$

In addition to a grid convergence study, a comparison is made between three cases. One case for a fine grid of 252 × 180 for which convergence is reached, secondly one on a coarse grid of 126×90 for which no convergence is reached and lastly one the same 126 × 90 coarse grid with one level of refinement. The variables of the simulation on the fine grid are given by Table 3. For the latter two cases all the variables on the coarse grid are the same apart from the time step and cell size of the coarsest cells, Δt and Δx, which are $3.205 \cdot 10^{-3}$ s and $7.056 \cdot 10^{-4}$ m. Note that for the case with one refinement α and ν are kept the same for the coarse grid cells and are rescaled for the refined cells in accordance with Equations 3.5 and 3.6. Besides are the results of the fully fine grid compared to other benchmark studies.

Table 3: Parameters used for cavity melting for no refinement

Variable	**Physical Meaning**	**value, unit**
L_x	Size in the x-direction	8.89 cm
L_y	Size in the y-direction	6.35 cm
N_x	Number of cells in the x-direction	252
N_y	Number of cells in the y-direction	180
Δx	Magnitude of coarsest cell	$3.532 \cdot 10^{-4}$ m
Δt	Magnitude of time step	$8.027 \cdot 10^{-4}$ s
α_{phys}	Physical value of the thermal diffusivity	$1.377 \cdot 10^{-5}$ m^2/s
α	Thermal diffuvisity in LB units	$8.862 \cdot 10^{-2} \Delta x^2/\Delta t$
ν_{phys}	Physical value of the viscosity	$2.971 \cdot 10^{-7}$ m^2/s
ν	Viscosity in LB units	$1.912 \cdot 10^{-3} \Delta x^2/\Delta t$
L	Latent heat	80160 J
C_p	Heat capacity	381.5 J/(kg K)
g_{grav}	Magnitude of the gravitational acceleration	9.8 m/s^{-2}
β_{exp}	Thermal expansion coefficient	$1.2 \cdot 10^{-4}$ K-1
Ste	Stefan number	0.0391
Ra	Rayleigh number	$6.052 \cdot 10^5$
Pr	Prandtl number	$2.158 \cdot 10^{-2}$
T_H	Hot wall temperature	38.00°C
T_C	Cold wall temperature	28.30°C
T_m	Melting point	29.78°C
T_0	Initial temperature	28.30°C
ϵ	Width of the mushy zone	0.0°C

4 Results

In this section the results of the simulations of the Stefan Problem will be discussed. For the Stefan problem this section mostly provides a proof of concept on the time savings gained from the mesh refinement. Besides that, the results are presented for the natural convection of air and cavity melting of tin, which are compared to other literature.

4.1 Stefan Problem

Section 6.1 of the Appendix shows the results for the simulations of the Stefan problem. Results are obtained of the temperature profile and melting front positions for a:

- 64×16 grid, no refinement (See Section 6.1.1);
- 32×8 main grid, one level of refinement (See Section 6.1.2);
- 32×8 main grid, no refinement (See Section 6.1.2);
- 16×4 main grid, two levels of refinement (See Section 6.1.4);
- 16×4 grid, no refinement (See Section 6.1.5);

In general all results match well with the theoretical values. As such is the refinement not implemented to improve the accuracy of the computations but rather to provide a proof of concept of saving computational time.

Looking at Figure 4.1 we see the temperature profile for one refinement on a 32×8 grid. The data is superimposed on the fine grid, meaning that a coarse grid cell is represented as two fine grid cells with equal value on the line of x-values. What can be seen, for instance looking at the line for $t = 10s$, are 5 single crosses just before the melting front. This means that the grid is fine in that area. On the left of that the values are double, which implies that those cells are coarse.

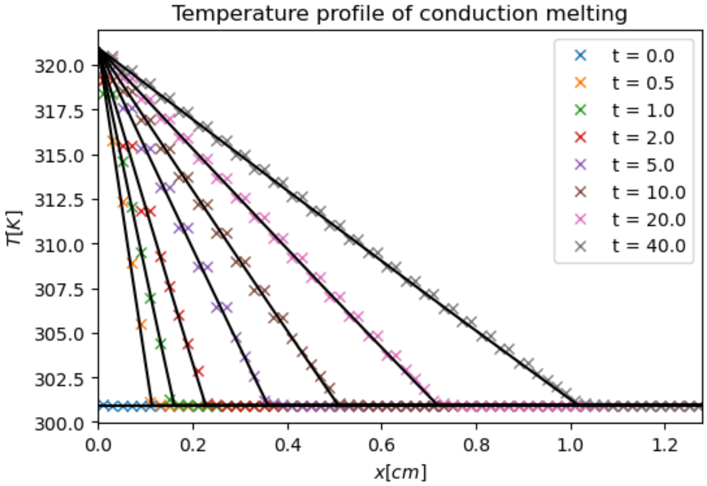

Figure 4.1: Simulated temperature profile vs analytical solution for a 32 × 8 grid and one level of refinement.

The same interpretation can be used to analyse the case for two refinements, see Figure 4.2. Again the temperature values are superimposed on the finest grid. Looking at the line for $t = 40s$ one can see two singular crosses just before the melting front, this is where the refinement is at level two. Left of that we see two pairs of double values, this is where the refinement is at level one. At the other cells left of that, we see pairs of four. This is where the grid is coarse.

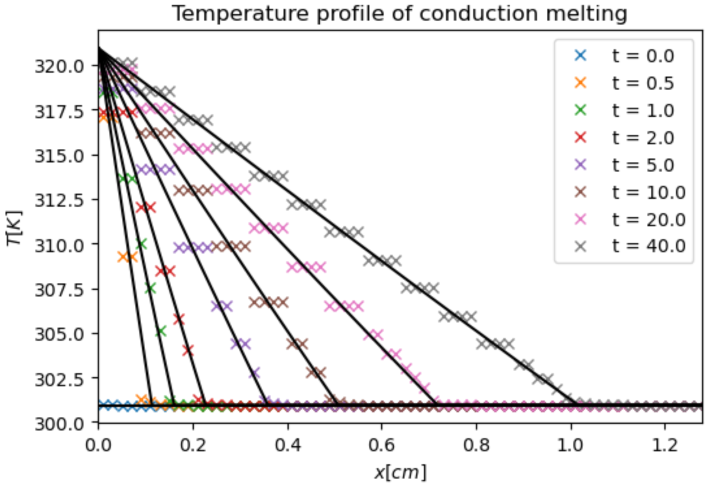

Figure 4.2: Simulated temperature profile vs analytical solution for a 16 × 4 grid and two levels of refinement.

4.1.1 Time Savings

In Table 4 the effect of using one level of refinement is given. Comparing a 32×8 grid to a 64×16 grid, both without refinement, one would ideally expect a factor 16 difference in computational time. As the there are 4 times more gridpoints in the fine grid and the time step is 4 times as small, as explained in Section 3.2.2. Here that is about 12.6. This is because this scaling law is not very accurate for smaller geometries since it does not consider that parallelization is not efficent for small data sizes.

Using a 32×8 grid with one refinement gives a reduction in computational time of 3.6 times. This however deviates quite a lot from the factor 12.6. This is firstly because the propagation step is performed on the fine grid, which means that for each time step two propagation steps need to be performed on the fine grid resulting in 8 times more computational expense for the propagation step. Secondly, we require more collision steps since on average 12.5% of the coarse cells are refined and each require 8 collision steps per time step. Lastly, is there 33.7% overhead in the calculations caused by averaging fine cells to coarse cells, which happens after the propagation step and splitting coarse cells into fine cells, which happens before propagation.

Table 4: Comparison of computational expense for a 64×16 grid, a 32×8 grid with one refinement and a a 32×8 grid without refinement. 'Refinement' specifies the percentage of coarse cells in each level of refinement, 'Overhead %' specifies the amount of overhead in the calculations caused by the AMR and 'Total' specifies the total computational time.

		One Refinement	
Dimensions	64 x 16	32 x 8	32 x 8
# of Refinements	0	1	0
Refinement level 0:	100.0%	87.5%	100.0%
level 1:		12.5%	
Overhead %	2.3%	33.7%	4.1%
Total (seconds)	371.59	104.47	28.46

Table 5 represents the savings in computational expense when two levels of refinement are used. For that matter a 64×16 grid has been compared to a 16×4 grid. Hypothetically should a 4 times coarser grid give a 256 smaller computational expense, as there are 16 times less gridpoints and the timestep is 16 times smaller (see Section 3.2.2). Again we see that this difference is less, 151.1 times. For two refinements the computational time is 9.9 times shorter compared to the fine grid. This again deviates a lot from just using a coarse grid for the same reasons as previously mentioned. However we do still see a significant reduction by using two levels of refinement instead of one.

Table 5: Comparison of computational expense for a 64 × 16 grid, a 16 × 4 grid with two levels of refinement and a a 16×4 grid without refinement. ’Refinement’ specifies the percentage of cells in each level of refinement, ’Overhead %’ specifies the amount of overhead in the calculations caused by the AMR and ’Total’ specifies the total computational time.

		Two Refinements		
Dimensions		64 x 16	16 x 4	16 x 4
# of Refinements		0	2	0
Refinement	level 0:	100.0%	79.5%	100.0%
	level 1:		12.5%	
	level 2:		8.1%	
Overhead %		2.3%	34.5%	9.7%
Total (seconds)		371.59	37.44	2.46

4.2 Natural Convection of Air

Initially it is determined for which grid size the solution converges. After which, it is investigated whether the converged grid can be made partially coarse with adaptive mesh refinement, yet yielding the same converged solution.

4.2.1 Grid Convergence

For a 30^2, 40^2, 45^2, 60^2, 76^2 and 90^2 grid the average, maximum and minimum Nusselt numbers are calculated on the cold wall, see Equation 3.19. These values can be found in Table 6 under ”Present (No Refinement)”. In addition to the Nusselt number the values of the maximum x-velocity on the central vertical line are given and the maximum y-velocity on the central horizontal line.

Table 6: Comparison of results for simulations of natural convection of air in a cavity. N_x specifies the size of the square grid, $u_{x,max}$ is the maximum x-component of the velocity on the vertical middle line in units of α/N_x, y is the y-position of this maximum. Similarly $u_{y,max}$ is the maximum y-component of the velocity on the horizontal middle line in units of α/N_x, x is the x-position of this maximum. Nu_{max} is the maximum Nusselt number on the cold wall and y_{Nu} the y-position of this maximum. Nu_{min}, Nu_{avg} are the minimum and average Nusselt number on the cold wall.
In the table we see the values by another study by Zhuo et al. [52], the present model for no refinement, the present model for one level of refinement based on the vorticity and the absolute value of the velocity.

Zhuo et al.

N_x	$u_{x,max}$	y	$u_{y,max}$	x	Nu_{max}	y_{Nu}	Nu_{min}	Nu_{avg}
59	34.81816	0.85593	67.89461	0.05932	7.66019	0.90678	0.73319	4.50307
119	34.75526	0.85294	68.50212	0.06303	7.70739	0.92017	0.72943	4.51775
239	34.74358	0.85565	68.61521	0.06485	7.71749	0.91841	0.72835	4.52078

Present (No refinement)

30	36.48588	0.83333	66.15523	0.06667	7.50799	0.86667	0.82905	4.42636
40	35.83754	0.85000	68.08506	0.05000	7.64289	0.90000	0.78587	4.48440
45	35.11937	0.84444	67.37750	0.06667	7.68202	0.88889	0.77258	4.49928
60	35.11937	0.85000	67.73321	0.05000	7.73802	0.90000	0.74834	4.52164
76	35.11937	0.85526	68.05201	0.06579	7.75973	0.90789	0.73496	4.53036
90	35.11937	0.85556	68.24862	0.05556	7.76684	0.91111	0.72795	4.53340

Present (One level of Refinement, ω)

45	35.48262	0.85000	67.46654	0.07222	7.88646	0.93333	0.74470	4.60657

Present (One level of Refinement, $|\vec{u}|$)

45	34.77736	0.85000	68.37225	0.05556	8.36675	0.94444	0.77044	4.54968

Figures 4.3a, 4.3b and 4.3c show that the average, minimum and maximum Nusselt number on the cold wall indeed converge at $N_x = 90$. Therefore it is interesting to see if similar results can be obtained on a 45^2 grid with adaptive mesh refinement.

Furthermore, the question is whether the numbers of the non-refined model are in good agreement with the numbers of Zhuo et al. [52]. This study also uses a double FMLB algorithm but uses the a finite difference to obtain the Nusselt number on the cold wall.

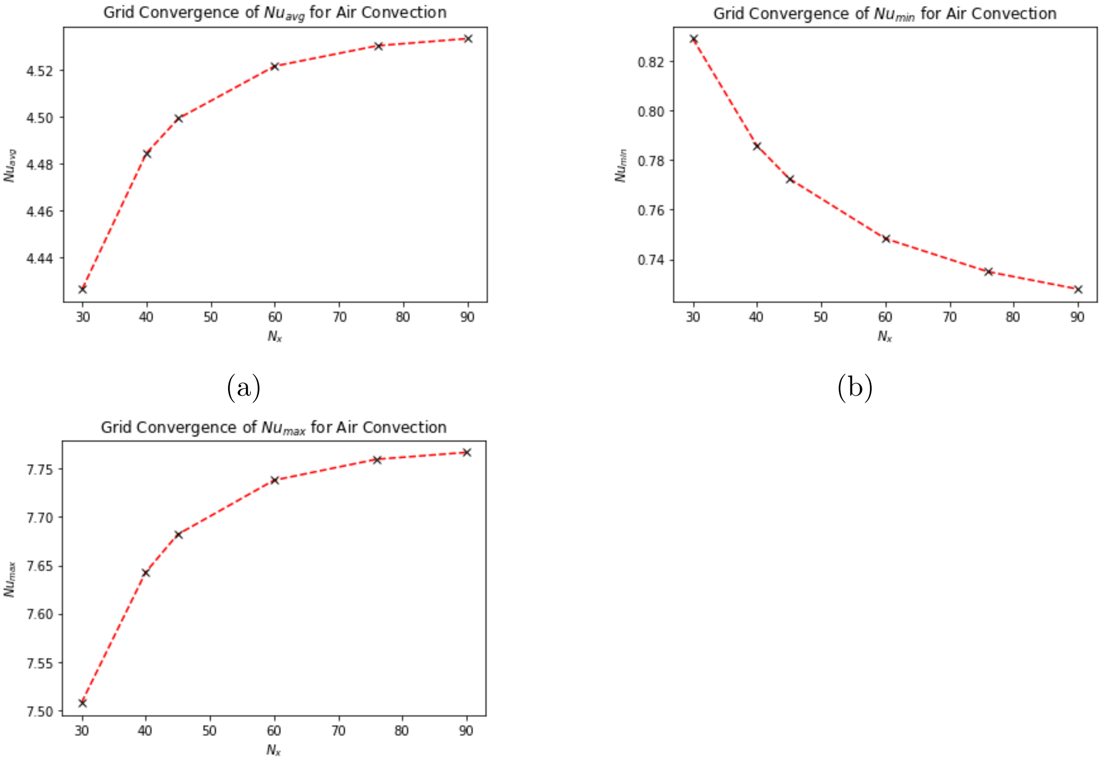

(a)

(b)

(c)

Figure 4.3: The value of the average Nusselt number on the cold wall versus the size of the grid given by N_x (a), the value of the minimum Nusselt number on the cold wall versus the size of the grid (b) and the value of the maximum Nusselt number on the cold wall versus the size of the grid (c).

4.2.2 Refinement Based on Vorticity

First we analyse the vorticity field without refinement, see Figure 4.4a. Based on this we choose $\omega_{upper} = 0.010$ $[\Delta t^{-1}]$ and $\omega_{lower} = 0.005$ $[\Delta t^{-1}]$ so that the area with higher vorticity is refined. It should be noted that the solution did not fully converge to a stable field. This could be due to the fact that the grid kept coarsening and refining.
Figures 4.4c through 4.4f show the results for the vorticiy, streamlines, refinement and absolute value of the temperature gradient. It can be seen that indeed the areas with higher vorticity are refined. In addition the pattern of the streamlines matches well with the case for no refinement, see Figure 4.4b.

However, we can also see discontinuities in the temperature gradient at the interface of the coarse and fine grid. In these simulations the solution is supposed to converge to a stable flow field where the vorticity field is also stable and thus the refinement area's are stable. In actuality certain parts of the domain kept coarsening and refining which could have impeded the temperature field from converging. Moreover, is the pattern in the vorticity not continuous at the interface between the coarse and fine grid; comparing the area inside the red boxes in Figure 4.4c to Figure 4.4a, the vorticity is smoother at the interface for the case of no refinement.

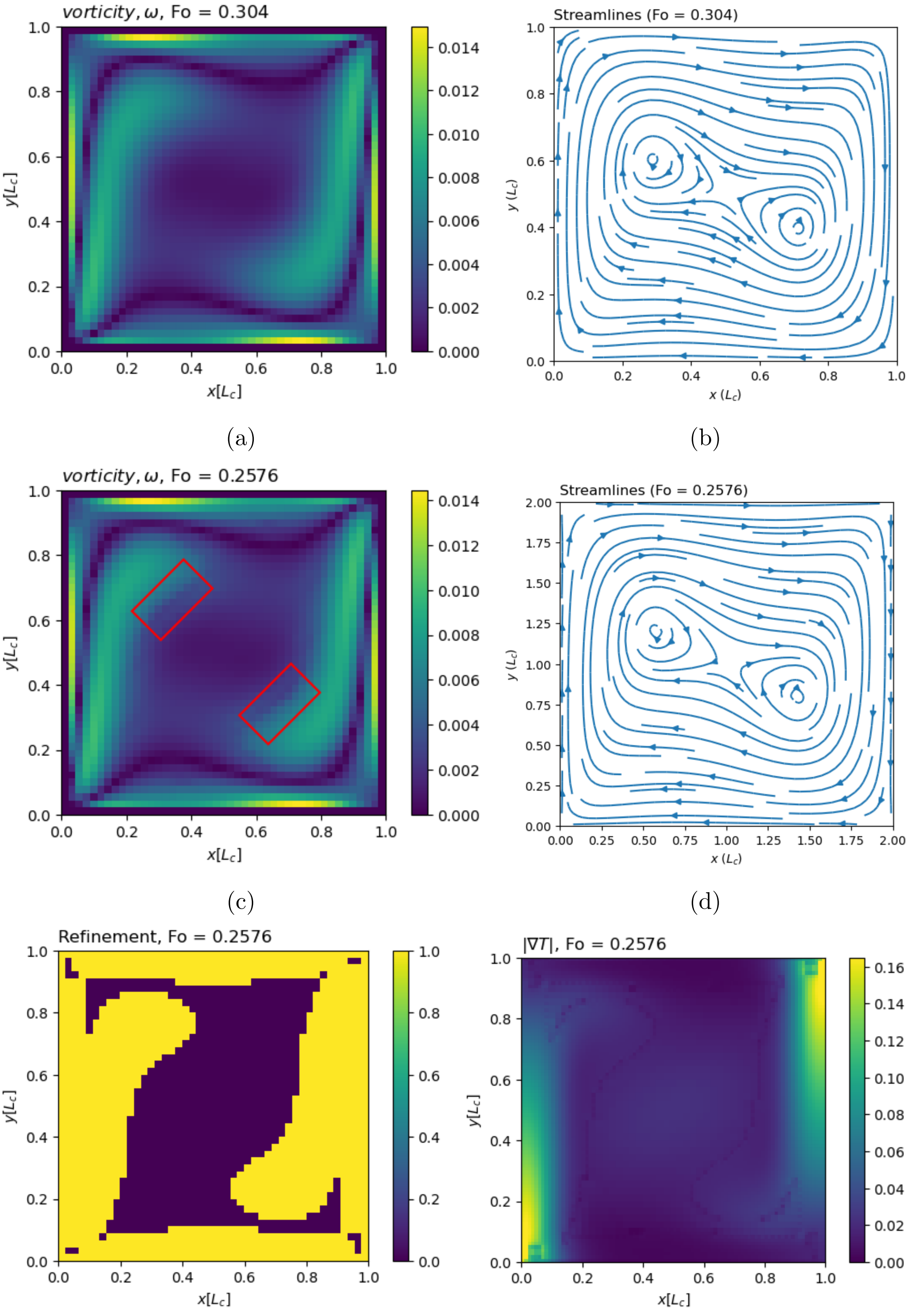

(a)

(b)

(c)

(d)

(e)

(f)

Figure 4.4: Figures a and b show the vorticity profile (a) and streamlines (b) for a 45^2 grid with no refinement. Figures c through f show the vorticity profile (c), streamlines (d), refinement profile (yellow = fine, blue = coarse) (e) and temperature gradient (f) for refinement based on the vorticity on a 45^2 grid.

4.2.3 Refinement Based on Absolute Velocity

Figures 4.5a through 4.5d show the results for the absolute velocity, streamlines, refinement and absolute value of the temperature gradient. Again, we see the discontinuity in the temperature gradient. The refinement is indeed applied in the area's where velocity is higher, in this case the threshold was set to 0.03 $\Delta x/\Delta t$. Comparing the data in Table 2 for refining based on vorticity and absolute velocity no concluding remarks can be made which more accurate, i.e. being similar to the case with a 90^2 grid.

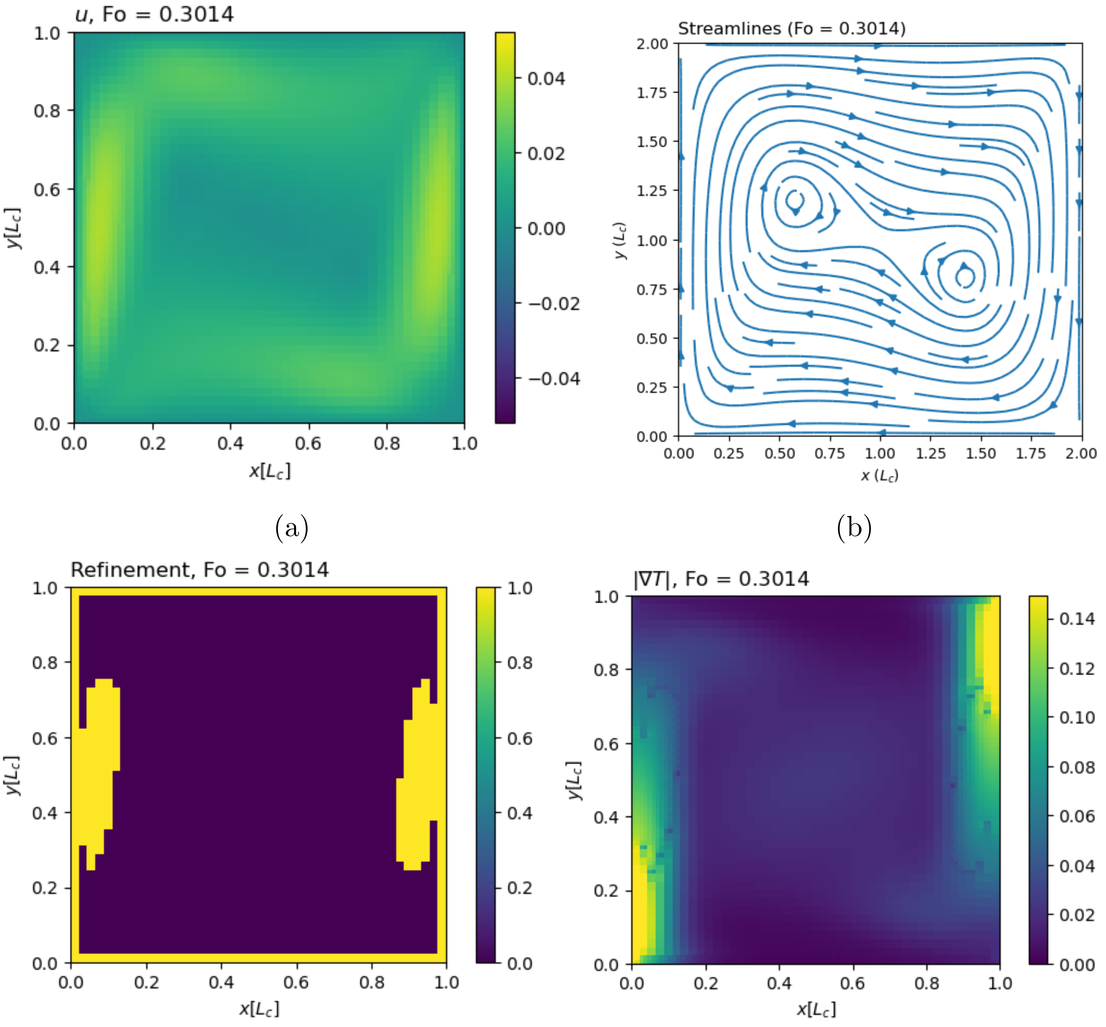

(a) (b)

(c) (d)

Figure 4.5: The absolute velocity profile (a), streamlines (b), refinement profile (yellow = fine, blue = coarse) (c) and temperature gradient (d) for refinement based on the absolute velocity on a 45^2 grid.

4.3 Convection Melting of Gallium

Firstly, a grid convergence study is taken using the melting front as a criterion for convergence. Secondly, is melting the front of the converged grid compared to similar benchmark studies. Lastly, is the influence of refinement investigated by comparing a fully coarse, fully fine and a partially refined grid in terms on accuracy and calculation time.

4.3.1 Grid Convergence

This study starts with an analysis on grid convergence. For this we define the melting front profile as indicator as it represents an accumulation of errors, which is also used in other studies [25, 29]. In Figure 4.6 we see the profiles for different grid sizes, with equal aspect ratio's. There is a relatively small difference between the melting front of the 252 × 180 grid and the 196 × 140 grid, which implies that the grid is converged or at least almost converged. Henceforth, the prior is chosen in further analysis on refinement.

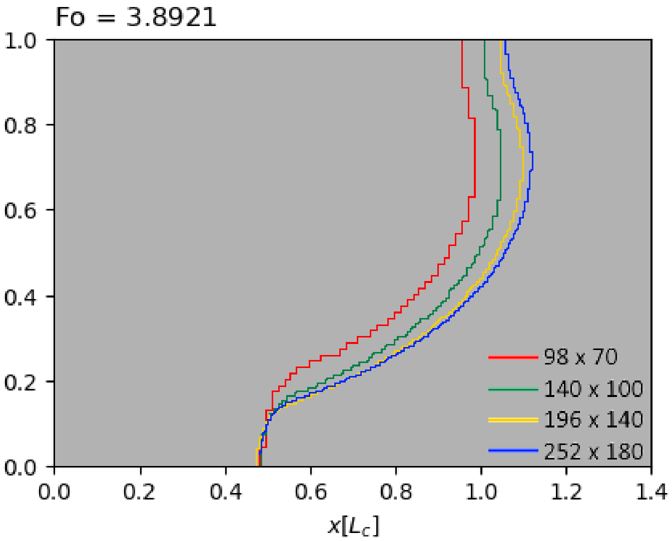

Figure 4.6: Grid convergence study for no refinement. The profiles represent the melting front after 19 minutes which corresponds to a Fourier number of 3.9821

4.3.2 Comparison Study

In order to validate the accuracy of the model, we compare the position of the melting front to other Benchmark studies for the exact same case, in 2D. The following studies have been chosen: Geadtke et al. which features a two-relaxation-time (TRT) double distributions LB model [13], a double distribution multiple-relaxation-time (MRT) model by Zhu et al. [51] and an OpenFOAM model based on the linearised enthalpy method by Reus [19]. One can see that all cases, apart from the TRT study by Geadtke match well. This might be beacuse, as aforementioned, a TRT models permits numerical heat diffusion causing inaccuracies. The fact that the model corresponds well with the MRT and OpenFOAM model further solidifies that the developed method for the latent heat implementation works correctly, also in a case where flow is involved.

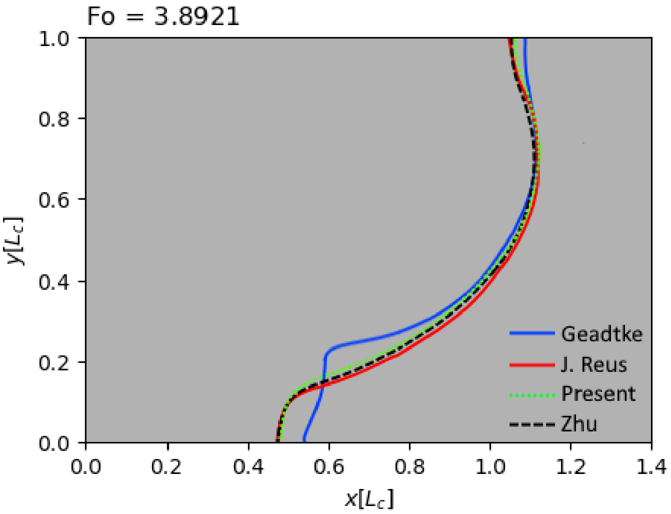

Figure 4.7: Comparison between melting fronts at 19 minutes for various benchmark studies. The model by Geadtke [13] is an SRT model, the study by Reus was done in OpenFOAM [19], the present model is for the case of a 252×180 grid and the model by Zhu [51] is a double MRT model.

4.3.3 Adaptive Mesh Refinement for Cavity Melting

The adaptive mesh refinement is investigated for different refinement criteria: the absolute velocity, the vorticity and the shear rate. For each criterion the melting front is compared to a fully coarse and a fully fine grid.

Another criterion one could think of is the temperature gradient, i.e. where one would refine if the temperature gradient would exceed a certain value. For a liquid metal like Gallium the Prandtl number is very low, which means that the temperature field quickly becomes rather smooth compared to the velocity field. This means that the high temperature gradients vanishes soon and this criterion has little added value.

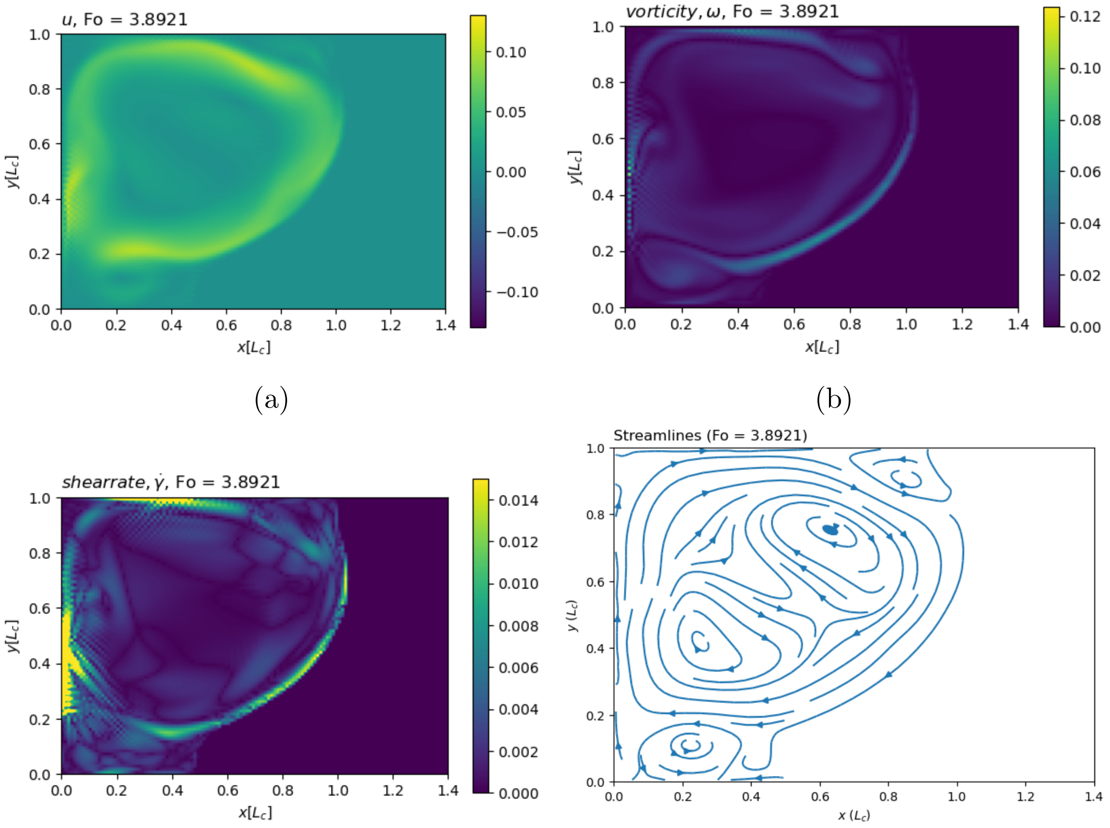

(a)

(b)

(c)

(d)

Figure 4.8: The absolute velocity profile (a), vorticity (b), shear rate (c) and streamlines (d) for a 126 × 90 coarse grid without refinement.

Adaptive Mesh Refinement Based on Absolute Velocity

Figure 4.9a shows a comparison of the melting fronts of a fully coarse grid, a coarse grid with adaptive mesh refinement based on the velocity and a fully fine grid. The chosen criterion for the velocity was $|\vec{u}| > 0.06\Delta x/\Delta t$. There is a rather large difference between the fully coarse case (126 × 90 grid) and the fully refined case (252 × 180 grid). This is because the grid is not converged yet at a grid size of 126 × 90, as shown in Figure 4.6. The results for one level of refinement are much better, but do not completely match the case for the fully refined grid at the bottom of the domain. In Figure 4.8b and Figure 4.9b we can see that the vorticity is high the bottom of the "belly" of the melting front, yet this area is not refined. This is however an area where the flow changes direction quite significantly judging from 4.8d.

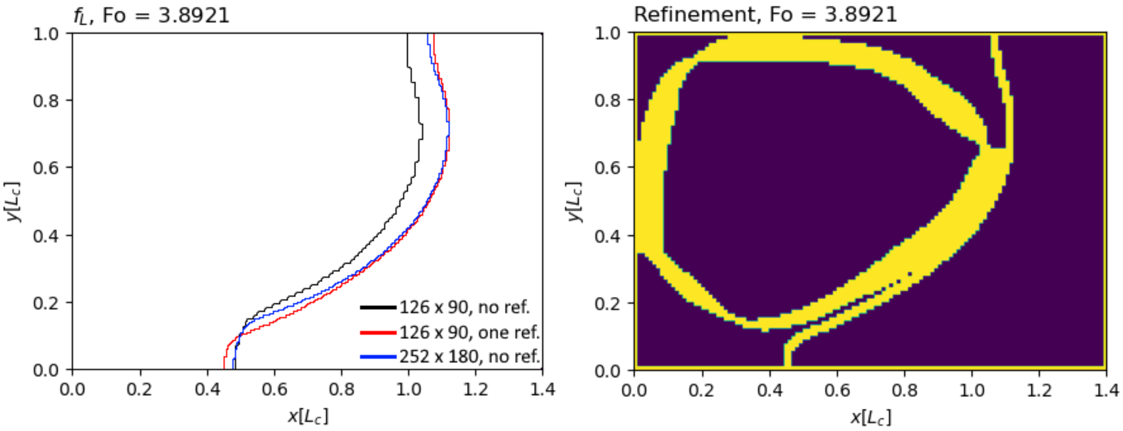

(a) (b)

Figure 4.9: Comparison between a fully coarse grid (black line, 126 × 90); a coarse grid with one refinement for high velocity areas, bounds and phase change region (red line, 126 × 90) and a fully fine grid (blue line, 252 × 180). The profiles represent the melting front after 19 minutes which corresponds to a Fourier number of 3.9821 (a). Representation of the grid fineness. Yellow marks the refined cells, blue marks the coarse cells (b).

Adaptive Mesh Refinement Based on Vorticity

Figure 4.10a shows the melting front for refinement based on a high vorticity. The criterion for the vorticity was $\omega_{upper} = 0.06\ \Delta t^{-1}$ and $\omega_{lower} = 0.03\ \Delta t^{-1}$. Figure 4.10b shows the refinement profile. Looking at Figure 4.8b it can be seen that the high vorticity area at the bottom of the "belly" of the melting front is indeed refined. Furthermore, does the profile of the melting front match well with the fully refined case.

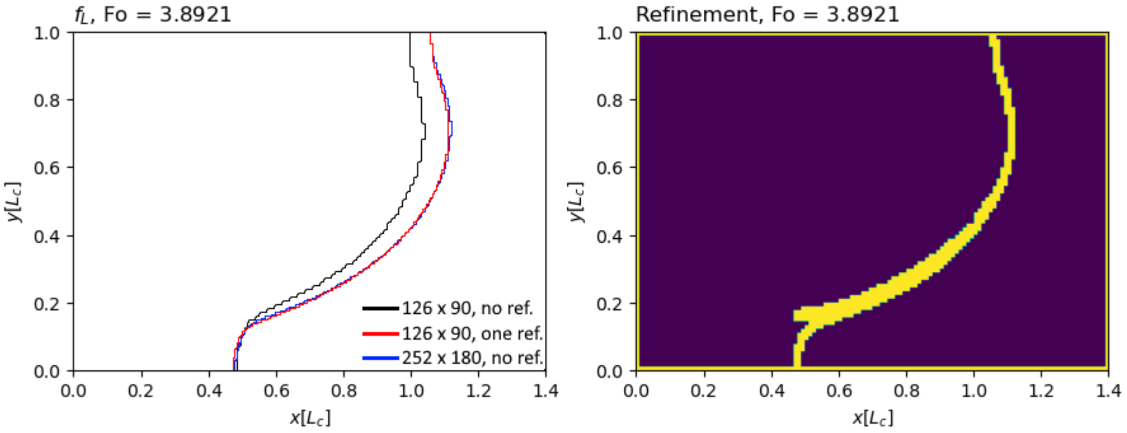

(a) (b)

Figure 4.10: Comparison between a fully coarse grid (black line, 126 × 90); a coarse grid with one refinement for high vorticity areas, bounds and phase change region (red line, 126 × 90) and a fully fine grid (blue line, 252 × 180). The profiles represent the melting front after 19 minutes which corresponds to a Fourier number of 3.9821 (a). Representation of the grid fineness. Yellow marks the refined cells, blue marks the coarse cells (b).

Adaptive Mesh Refinement Based on Shear Rate

The results for the last criterion are given in Figures 4.11a and 4.11b. Indeed the areas of high shear rate are refined. However the refinement criterion might be too strict. The threshold for refinement for the shear rate was set to $\dot{\gamma}$ >0.0025 Δt^{-1}. From Figures 4.8b and 4.8c one can see that the high shear rate area and high vorticity area overlap at the bottom of the belly of the melting front. This suggests that a looser criterion on the shear rate that guarantees that this area is at least refined is probably also sufficient. This would decrease the number of cells that need to be refined with consequentially saving computational time. Just like the case for the refinement based on vorticity, the melting front for refinement based on the shear rate matches well with the fully fine grid, see Figure 4.11a.

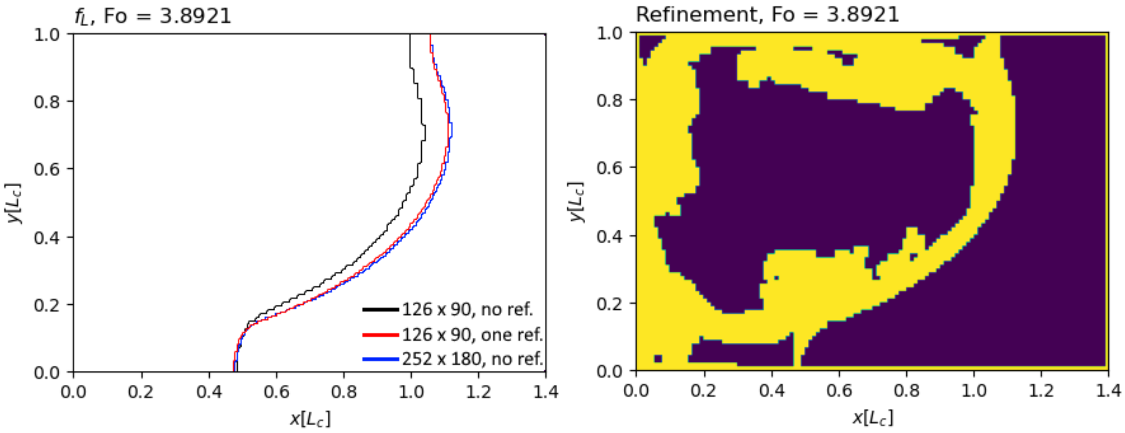

(a)

(b)

Figure 4.11: Comparison between a fully coarse grid (black line, 126 × 90); a coarse grid with one refinement for high shear rate areas, bounds and phase change region (red line, 126 × 90) and a fully fine grid (blue line, 252 × 180). The profiles represent the melting front after 19 minutes which corresponds to a Fourier number of 3.9821 (a). Representation of the grid fineness. Yellow marks the refined cells, blue marks the coarse cells (b).

4.3.4 Computational Time

Table 7 shows the results for the computational time for a fully fine grid, a fully coarse grid and the cases for adaptive mesh refinement based on the velocity, vorticity and shear rate. All three criteria lead to a grid which mostly consists of coarse cells, which gives a reduction of about 3 to 4 times in computational expense. Comparing the three refinement criteria we see that a higher percentage of fine cells leads to more computational time, as expected. The refining based on the shear rate is significantly more expensive than refining based the vorticity. As aforementioned, the prior would be cheaper if a looser criterion would have been used.

The fact that the results for the vorticity are very close to the fully fine grid, with so little refined cells, does not necessarily mean it is a superior criterion to the shear rate. In fact, the vorticity only captures the rotation in the velocity field but does not capture areas with high velocity gradients: $\partial u_x/\partial u_x$ and $\partial u_y/\partial u_y$. The shear rate, in the contrary, does capture these.

Table 7: Computational time for a case with a fine grid of 252 × 180 (first column), a case for a coarse grid of 126 × 90 with one refinement level based on the velocity (second column), a case for a coarse grid of 126 × 90 with one refinement level based on the vorticity (third column), a case for a coarse grid of 126 × 90 with one refinement level based on the shear rate (fourth column) and a case for a 126 × 90 grid with no refinement (fifth column). 'Refinement' specifies the percentage of cells in each level of refinement, 'Overhead %' specifies the amount of overhead in the calculations caused by the AMR and 'Total' specifies the total computational time.

			Simulations		
Dimensions	252 × 180	126 × 90	126 × 90	126 × 90	126 × 90
# of Refinements	0	1	1	1	0
Criterion		Velocity	Vorticity	Shear rate	
Refinement level 0:	100.0%	90.2%	93.1%	71.9%	100.0%
level 1:		9.8%	6.9%	28.1%	
overhead %	0.67%	8.88%	6.06%	4.79%	0.95%
overhead time (hours)	0.42	1.66	1.00	1.03	0.03
col and prop (hours)	62.45	17.01	15.42	20.50	3.65
total (hours)	62.86	18.67	16.42	21.53	3.68

5 conclusion

The aims of this research were: to find a way to implement the latent in the FMLB scheme, quantify the time reduction from using AMR in the Stefan Problem and investigating criteria for AMR in convection melting in terms of computational time and accuracy. All of this in the broader purpose to improve modeling of convection melting. The methodology was tested by simulating benchmarks and comparing the results to literature, which were: the Stefan Problem, natural convection of air in a square cavity and convection melting in a rectangular cavity.

The first issue was solved by separating the total enthalpy in a latent heat part and sensible heat part. The collision operation would only be applied to the sensible heat after which the latent heat was added again to obtain the post-collision distribution for the enthalpy. The results from the Stefan Problem simulation show that this implementation works as they match the theoretical solution.

In addition, did the simulations on the Stefan Problem also show potential for time reduction, which was the second aim. By refining the phase change region a significant reduction compared to a fully fine grid was found. For a single refinement this amounted to ~ 3.6 times and for two refinements ~ 9.9 times.

Before testing the AMR criteria for the convection melting case, it was validated that the grid-converged case on a fully fine grid matched well with other literature. After which, three criteria for refinement were studied: absolute velocity, vorticity and the shear rate. The latter two delivered a solution with similar melting front to the fully fine grid. However, the velocity criterion was not effective on refining key areas of the domain where the flow changed direction and as such the melting front deviated. All three criteria led to a reduction in calculation time of about 3-4 times. In this specific case the vorticity could be a more efficient criterion since it requires less cells to be refined. Be that as it may, it only captures regions where the flow strongly changes direction but ignores certain regions with high velocity gradients. For that reason the shear rate might still be a more reliable criterion.

Besides the current implementation of mesh refinement, there is still room for improvement. In this research the streaming step was performed on the finest grid only. Which means that for a higher refinement levels the streaming impedes the savings in computational time. This could be fixed by applying the methodology of Rohde et al. [34], where the coarser cells need not to be temporarily refined for the streaming. Another interesting topic for the refinement scheme is to use curve-linear coordinates, see the thesis by Reyes Barrazza [3]. Here certain parts of the domain can be made fine by locally contracting the grid.

References

[1] R. Gooya et al. "A new coupled pore-scale Lattice Boltzmann Method with PhreeqcRM (LAMP)". In: (2016).

[2] Inc ANSYS. 2022. URL: `https://www.ansys.com/`.

[3] Juan Reyes Barraza. "A generalised lattice Boltzmann method with block-structured adaptive mesh refinement". Parts of this work have been published as: J. A. Reyes Barraza and R. Deiterding. A Lattice Boltzmann method in generalized curvilinear coordinates, pages 477?488. International Centre for Numerical Methods in Engineering (CIMNE), 2019 J. A. Reyes Barraza and R. Deiterding. Towards a generalised lattice Boltzmann method for aerodynamic simulations. Journal of Computational Science, 45:101182, 2020. PhD thesis. University of Southampton, Nov. 2021. URL: `https://eprints.soton.ac.uk/457805/`.

[4] Adrian Bejan. *1.3 First Law of Thermodynamics.* 2013. URL: `https://app.knovel.com/hotlink/khtml/id:kt011B6VH3/convection-heat-transfer/first-law-thermodynamics`.

[5] SUMAN CHAKRABORTY and DIPANKAR CHATTERJEE. "An enthalpy-based hybrid lattice-Boltzmann method for modelling solid–liquid phase transition in the presence of convective transport". In: *Journal of Fluid Mechanics* 592 (2007), pp. 155–175. DOI: `10.1017/S0022112007008555`.

[6] *Climate Change and Nuclear Power 2020.* Non-serial Publications. Vienna: INTERNATIONAL ATOMIC ENERGY AGENCY, 2020. ISBN: 978-92-0-115020-2. URL: `https://www.iaea.org/publications/14725/climate-change-and-nuclear-power-2020`.

[7] *Computer Codes.* 2021. URL: `https://www.nrc.gov/about-nrc/regulatory/research/safetycodes.html`.

[8] COMSOL. 2022. URL: `https://www.comsol.com/`.

[9] J.G.M. Eggels and J.A. Somers. "Numerical simulation of free convective flow using the lattice-Boltzmann scheme". In: *International Journal of Heat and Fluid Flow* 16.5 (1995), pp. 357–364. ISSN: 0142-727X. DOI: `https://doi.org/10.1016/0142-727X(95)00052-R`. URL: `https://www.sciencedirect.com/science/article/pii/0142727X9500052R`.

[10] Mohsen Eshraghi and Sergio D. Felicelli. "An implicit lattice Boltzmann model for heat conduction with phase change". In: *International Journal of Heat and Mass Transfer* 55.9 (2012), pp. 2420–2428. ISSN: 0017-9310. DOI: `https://doi.org/10.1016/j.ijheatmasstransfer.2012.01.`

018. URL: https://www.sciencedirect.com/science/article/pii/S0017931012000191.

[11] Moritz Faden, Andreas König-Haagen, and Dieter Brüggemann. "An Optimum Enthalpy Approach for Melting and Solidification with Volume Change". In: (Jan. 2019). DOI: 10.15495/EPub_UBT_00004649.

[12] Abbas Fakhari and Taehun Lee. "Finite-difference lattice Boltzmann method with a block-structured adaptive-mesh-refinement technique". In: *Physical review. E, Statistical, nonlinear, and soft matter physics* 89 (Mar. 2014), p. 033310. DOI: 10.1103/PhysRevE.89.033310.

[13] Maximilian Gaedtke et al. "Total enthalpy-based lattice Boltzmann simulations of melting in paraffin/metal foam composite phase change materials". In: *International Journal of Heat and Mass Transfer* 155 (2020), p. 119870. ISSN: 0017-9310. DOI: https://doi.org/10.1016/j.ijheatmasstransfer.2020.119870. URL: https://www.sciencedirect.com/science/article/pii/S0017931019361927.

[14] Davood Domairry Ganji and Sayyid Habibollah Hashemi Kachapi. "Chapter 6 - Natural, Mixed, and Forced Convection in Nanofluid". In: *Application of Nonlinear Systems in Nanomechanics and Nanofluids*. Ed. by Davood Domairry Ganji and Sayyid Habibollah Hashemi Kachapi. Micro and Nano Technologies. Oxford: William Andrew Publishing, 2015, pp. 205–269. ISBN: 978-0-323-35237-6. DOI: https://doi.org/10.1016/B978-0-323-35237-6.00006-6. URL: https://www.sciencedirect.com/science/article/pii/B9780323352376000066.

[15] *Generation IV Systems*. URL: https://www.gen-4.org/gif/jcms/c_40465/generation-iv-systems.

[16] Stephen M. Goldberg and Robert Rosner. *Nuclear Reactors: Generation to Generation*. 2011. URL: https://www.amacad.org/sites/default/files/academy/pdfs/nuclearReactors.pdf.

[17] Rongzong Huang and Huiying Wu. "Phase interface effects in the total enthalpy-based lattice Boltzmann model for solid–liquid phase change". In: *Journal of Computational Physics* 294 (2015), pp. 346–362. ISSN: 0021-9991. DOI: https://doi.org/10.1016/j.jcp.2015.03.064. URL: https://www.sciencedirect.com/science/article/pii/S0021999115002259.

[18] Rongzong Huang, Huiying Wu, and Ping Cheng. "A new lattice Boltzmann model for solid–liquid phase change". In: *International Journal of Heat and Mass Transfer* 59 (2013), pp. 295–301. ISSN: 0017-9310. DOI: https://doi.org/10.1016/j.ijheatmasstransfer.2012.12.027. URL: https://www.sciencedirect.com/science/article/pii/S0017931012009830.

[19] Reus. J. “A Numerical Investigation of Freeze-Valve Melting based on a Linearised Enthalpy Method”. In: (Aug. 2021).

[20] Mohammed Jami et al. “New thermal MRT lattice Boltzmann method for simulations of convective flows”. In: *International Journal of Thermal Sciences* 100 (2016), pp. 98–107. ISSN: 1290-0729. DOI: `https://doi.org/10.1016/j.ijthermalsci.2015.09.011`. URL: `https://www.sciencedirect.com/science/article/pii/S1290072915002720`.

[21] M.D. Kelleher et al. “SCIENTIFIC COMMITTEE”. In: *Experimental Heat Transfer, Fluid Mechanics and Thermodynamics 1993*. Ed. by M.D. Kelleher et al. Elsevier Series in Thermal and Fluid Sciences. Amsterdam: Elsevier, 1993, pp. vii–viii. ISBN: 978-0-444-81619-1. DOI: `https://doi.org/10.1016/B978-0-444-81619-1.50004-6`. URL: `https://www.sciencedirect.com/science/article/pii/B9780444816191500046`.

[22] Abdelghani Laouer et al. “Study of Natural Convection Melting of Phase Change Material inside a Rectangular Cavity with Non-Uniformly Heated Wall”. In: *Defect and Diffusion Forum* 406 (Feb. 2021), pp. 3–11. DOI: `10.4028/www.scientific.net/DDF.406.3`.

[23] Dinggen Li and Zihao Yu. “Natural convection melting in a cubic cavity with internal fins: A lattice Boltzmann study”. In: *Case Studies in Thermal Engineering* 25 (2021), p. 100919. ISSN: 2214-157X. DOI: `https://doi.org/10.1016/j.csite.2021.100919`. URL: `https://www.sciencedirect.com/science/article/pii/S2214157X21000824`.

[24] Qing Liu and Ya-Ling He. “Double multiple-relaxation-time lattice Boltzmann model for solid–liquid phase change with natural convection in porous media”. In: *Physica A: Statistical Mechanics and its Applications* 438 (2015), pp. 94–106. ISSN: 0378-4371. DOI: `https://doi.org/10.1016/j.physa.2015.06.018`. URL: `https://www.sciencedirect.com/science/article/pii/S0378437115005713`.

[25] J. Lopez. “Master thesis : Implementation of a melting/solidification process with the enthalpy method”. In: ().

[26] Riheb Mabrouk et al. “On Numerical Modeling of Thermal Performance Enhancementof a Heat Thermal Energy Storage System Using a Phase Change Material and a Porous Foam”. In: *Computation* 10.1 (2022). ISSN: 2079-3197. DOI: `10.3390/computation10010003`. URL: `https://www.mdpi.com/2079-3197/10/1/3`.

[27] Elsa Merle. *Concept of Molten Salt Fast Reactor*. URL: `https://www.gen-4.org/gif/upload/docs/application/pdf/2017-05/07_elsa_merle_france.pdf`.

[28] Philipp Neumann et al. “A Coupled Approach for Fluid Dynamic Problems Using the PDE Framework Peano”. In: *Communications in Computational Physics* 12 (July 2012). DOI: 10.4208/cicp.210910.200611a.

[29] Hannoun Noureddine, V. Alexiades, and Tsun Mai. “Resolving the controversy of gallium and tin melting in a rectangular cavity heated from the side”. In: *Numerical Heat Transfer Fundamentals* B44 (Sept. 2003), pp. 253–276. DOI: 10.1080/10407790390226974.

[30] OpenCFD. 2022. URL: https://www.openfoam.com/.

[31] Stéphane Popinet. “Gerris: a tree-based adaptive solver for the incompressible Euler equations in complex geometries”. In: *Journal of Computational Physics* 190.2 (2003), pp. 572–600. ISSN: 0021-9991. DOI: https://doi.org/10.1016/S0021-9991(03)00298-5. URL: https://www.sciencedirect.com/science/article/pii/S0021999103002985.

[32] J. Reddy. “Principles of Continuum Mechanics: A Study of Conservation Principles with Applications”. In: 2010.

[33] David Reinberger, Amela Ajanovic, and Reinhard Haas. *The Technological Development of Diferent Generations and Reactor Concepts.* 2019. URL: https://link.springer.com/content/pdf/10.1007/978-3-658-25987-7_11.pdf.

[34] M. Rohde et al. “A generic, mass conservative local grid refinement technique for lattice-Boltzmann schemes”. In: *International Journal for Numerical Methods in Fluids* 51.4 (2006), pp. 439–468. DOI: https://doi.org/10.1002/fld.1140. eprint: https://onlinelibrary.wiley.com/doi/pdf/10.1002/fld.1140. URL: https://onlinelibrary.wiley.com/doi/abs/10.1002/fld.1140.

[35] Rubiolo, Pablo R. et al. “High temperature thermal hydraulics modeling of a molten salt: application to a molten salt fast reactor (MSFR) ***”. In: *ESAIM: ProcS* 58 (2017), pp. 98–117. DOI: 10.1051/proc/201758098. URL: https://doi.org/10.1051/proc/201758098.

[36] Gamboa Palacios S and J. Jansen. *Nuclear energy economics: An update to Fact Finding Nuclear Energy.* 2018. URL: https://energy.nl/wp-content/uploads/2019/06/TNO-2018-P11577.pdf.

[37] Erik M. Salomons, Walter J. A. Lohman, and Han Zhou. “Simulation of Sound Waves Using the Lattice Boltzmann Method for Fluid Flow: Benchmark Cases for Outdoor Sound Propagation”. In: *PLOS ONE* 11.1 (Jan. 2016), pp. 1–19. DOI: 10.1371/journal.pone.0147206. URL: https://doi.org/10.1371/journal.pone.0147206.

[38] Xiaowen Shan. “Simulation of Rayleigh-Bénard convection using a lattice Boltzmann method”. In: *Phys. Rev. E* 55 (3 Mar. 1997), pp. 2780–2788. DOI: 10.1103/PhysRevE.55.2780. URL: https://link.aps.org/doi/10.1103/PhysRevE.55.2780.

[39] P.R. Shukla et al. *Summary for Policymakers. In: Climate Change and Land: an IPCC special report on climate change, desertification, land degradation, sustainable land management, food security, and greenhouse gas fluxes in terrestrial ecosystems.* In Press, 2018. URL: https://www.ipcc.ch/site/assets/uploads/sites/2/2019/05/SR15_Approval_Doc.-2a-Rev.-1-Final-Draft-SPM.pdf.

[40] C. Swaminathan and V. Voller. “ON THE ENTHALPY METHOD”. In: *International Journal of Numerical Methods for Heat & Fluid Flow* 3 (1993), pp. 233–244.

[41] *The History of Nuclear Energy.* URL: https://www.energy.gov/sites/prod/files/The20History20of20Nuclear20Energy_0.pdf.

[42] Jos Thijssen. *Computational Physics.* 2nd ed. Cambridge University Press, 2007. DOI: 10.1017/CBO9781139171397.

[43] Patrik Thollander et al. “2 - General energy theory11Parts of this section are based on Areskoug and Eliasson (2011).” In: *Introduction to Industrial Energy Efficiency.* Ed. by Patrik Thollander et al. Academic Press, 2020, pp. 15–30. ISBN: 978-0-12-817247-6. DOI: https://doi.org/10.1016/B978-0-12-817247-6.00002-X. URL: https://www.sciencedirect.com/science/article/pii/B978012817247600002X.

[44] Marco Tiberga et al. “Preliminary investigation on the melting behavior of a freeze-valve for the Molten Salt Fast Reactor”. In: *Annals of Nuclear Energy* 132 (June 2019), pp. 544–554. DOI: 10.1016/j.anucene.2019.06.039.

[45] Krüger Timm et al. “The lattice Boltzmann method: principles and practice”. In: *Springer International Publishing AG Switzerland, ISSN* (2016), pp. 1868–4521.

[46] Jiyuan Tu, Guan-Heng Yeoh, and Chaoqun Liu. “Chapter 9 - Some Advanced Topics in CFD”. In: *Computational Fluid Dynamics (Third Edition).* Ed. by Jiyuan Tu, Guan-Heng Yeoh, and Chaoqun Liu. Third Edition. Butterworth-Heinemann, 2018, pp. 369–417. ISBN: 978-0-08-101127-0. DOI: https://doi.org/10.1016/B978-0-08-101127-0.00009-X. URL: https://www.sciencedirect.com/science/article/pii/B978008101127000009X.

[47] Vasily Vasil'ev and Maria Vasilyeva. "An Accurate Approximation of the Two-Phase Stefan Problem with Coefficient Smoothing". In: *Mathematics* 8.11 (2020). ISSN: 2227-7390. DOI: `10.3390/math8111924`. URL: `https://www.mdpi.com/2227-7390/8/11/1924`.

[48] Jesper van Winden. *Developing a Hybrid Lattice Boltzmann Finite Difference Model for Phase Change in the Molten Salt Reactor.* 2021. URL: `http://repository.tudelft.nl/`.

[49] Fan Yang et al. "MRT Lattice Boltzmann Schemes for High Reynolds Number Flow in Two-Dimensional Lid-Driven Semi-Circular Cavity". In: *Energy Procedia* 16 (2012). 2012 International Conference on Future Energy, Environment, and Materials, pp. 639–644. ISSN: 1876-6102. DOI: `https://doi.org/10.1016/j.egypro.2012.01.103`. URL: `https://www.sciencedirect.com/science/article/pii/S1876610212001130`.

[50] Ting Zhang et al. "General bounce-back scheme for concentration boundary condition in the lattice-Boltzmann method". In: *Phys. Rev. E* 85 (1 Jan. 2012), p. 016701. DOI: `10.1103/PhysRevE.85.016701`. URL: `https://link.aps.org/doi/10.1103/PhysRevE.85.016701`.

[51] Weibing Zhu, Meng Wang, and Hong Chen. "2D and 3D lattice Boltzmann simulation for natural convection melting". In: *International Journal of Thermal Sciences* 117 (2017), pp. 239–250. ISSN: 1290-0729. DOI: `https://doi.org/10.1016/j.ijthermalsci.2017.03.025`. URL: `https://www.sciencedirect.com/science/article/pii/S1290072916309231`.

[52] Congshan Zhuo, Chengwen Zhong, and Jun Cao. "Filter-matrix lattice Boltzmann model for incompressible thermal flows". In: *Phys. Rev. E* 85 (4 Apr. 2012), p. 046703. DOI: `10.1103/PhysRevE.85.046703`. URL: `https://link.aps.org/doi/10.1103/PhysRevE.85.046703`.

[53] Congshan Zhuo, Chengwen Zhong, and Jun Cao. "Filter-matrix lattice Boltzmann simulation of lid-driven deep-cavity flows, Part I — Steady flows". In: *Computers and Mathematics with Applications* 65.12 (2013), pp. 1863–1882. ISSN: 0898-1221. DOI: `https://doi.org/10.1016/j.camwa.2013.02.020`. URL: `https://www.sciencedirect.com/science/article/pii/S0898122113001429`.

[54] Bahman Zohuri. "6 - Generation IV nuclear reactors". In: *Nuclear Reactor Technology Development and Utilization.* Ed. by Salah Ud-Din Khan and Alexander Nakhabov. Woodhead Publishing Series in Energy. Woodhead Publishing, 2020, pp. 213–246. ISBN: 978-0-12-818483-7. DOI: `https://doi.org/10.1016/B978-0-12-818483-7.00006-8`. URL: `https://www.sciencedirect.com/science/article/pii/B9780128184837000068`.

5.0.1 Contributioms

The most important contributions of this researsch were:

- Finding a computationally efficient method to implement the latent heat of melting in the thermal scheme for the Filter-Matrix method, using a source-based implementation.
- Quantifying the reduction of computational time through applying adaptive mesh refinement on the Stefan Problem, where the phase change region was tracked and refined.
- Performing simulations on the cavity melting of gallium using a double-distribution Filter Matrix scheme, enthalpy porosity method and the efficient source based implementation of the latent heat.
- Comparing the absolute value of the velocity, vorticity and shear rate as criteria for convection melting of gallium in terms of computational expense and accuracy.

5.0.2 Code Repository

The code for this project is written in python and mostly parallelized in using the Numba package. The code can be found on: `https://gitlab.tudelft.nl/mrohde/msc-project-thorben-besseling.git`, or use the QR code:

6 Appendix

6.0.1 Structure of the Algorithm

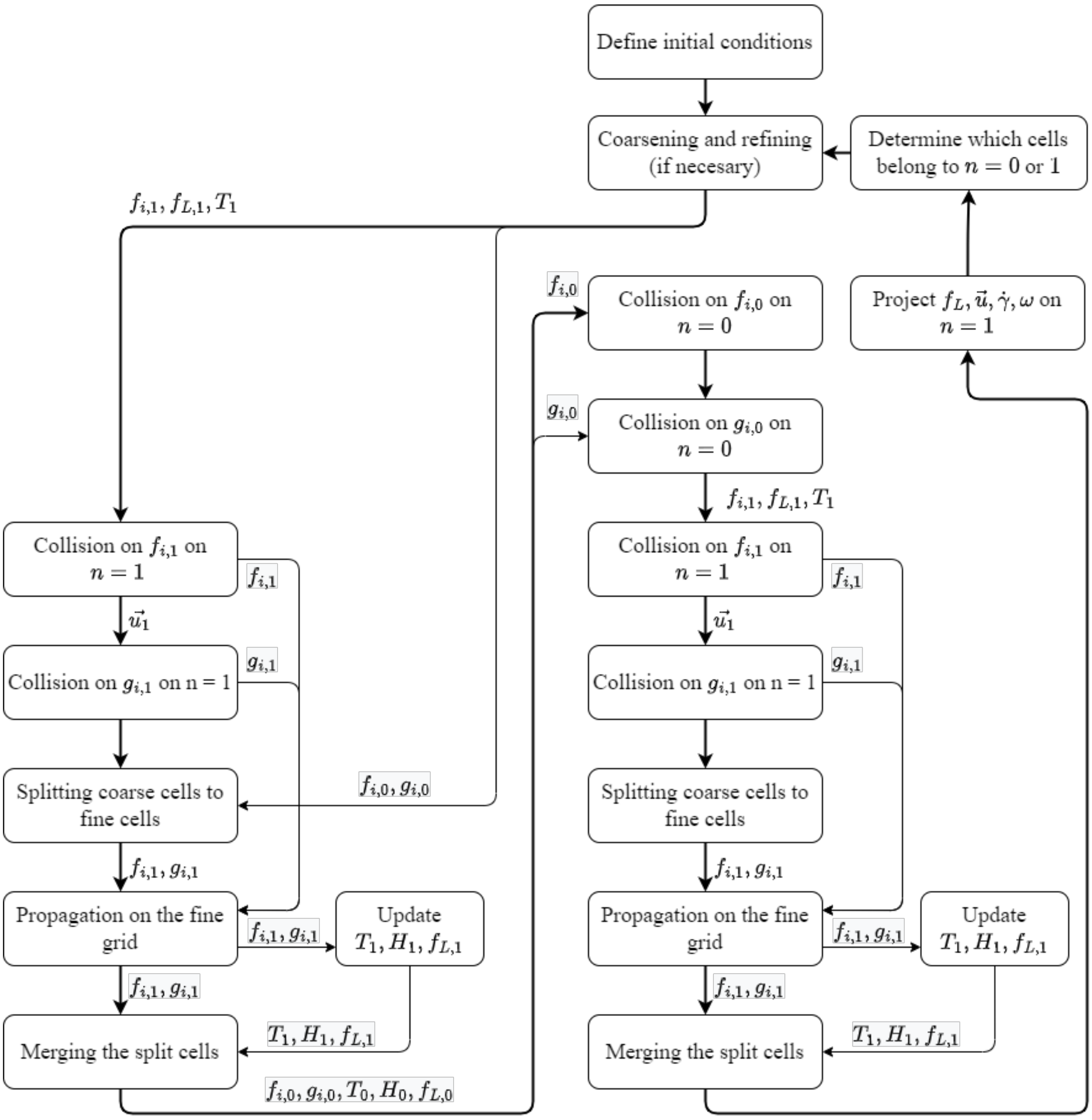
Define initial conditions
Coarsening and refining (if necesary)
Determine which cells belong to $n = 0$ or 1
$f_{i,1}, f_{L,1}, T_1$
$f_{i,0}$
Collision on $f_{i,0}$ on $n = 0$
Project $f_L, \vec{u}, \dot{\gamma}, \omega$ on $n = 1$
$g_{i,0}$
Collision on $g_{i,0}$ on $n = 0$
$f_{i,1}, f_{L,1}, T_1$
Collision on $f_{i,1}$ on $n = 1$
$f_{i,1}$
$\vec{u_1}$
Collision on $g_{i,1}$ on n = 1
$g_{i,1}$
Splitting coarse cells to fine cells
$f_{i,0}, g_{i,0}$
$f_{i,1}, g_{i,1}$
Propagation on the fine grid
$f_{i,1}, g_{i,1}$
Update $T_1, H_1, f_{L,1}$
$f_{i,1}, g_{i,1}$
Merging the split cells
$T_1, H_1, f_{L,1}$
$f_{i,0}, g_{i,0}, T_0, H_0, f_{L,0}$
Collision on $f_{i,1}$ on $n = 1$
$f_{i,1}$
$\vec{u_1}$
Collision on $g_{i,1}$ on n = 1
$g_{i,1}$
Splitting coarse cells to fine cells
$f_{i,1}, g_{i,1}$
Propagation on the fine grid
$f_{i,1}, g_{i,1}$
Update $T_1, H_1, f_{L,1}$
$f_{i,1}, g_{i,1}$
Merging the split cells
$T_1, H_1, f_{L,1}$

Figure 6.1: Structure of the algorithm. The thick arrows mark the order of operations through the algorithm, the thin arrows mark the inputs and outputs of data and the subscripts mark whether a variable is on the coarse grid (n = 0) or fine grid (n = 1).

6.1 Results Stefan Problem

6.1.1 $N_x = 64$, $N_y = 16$, no refinement

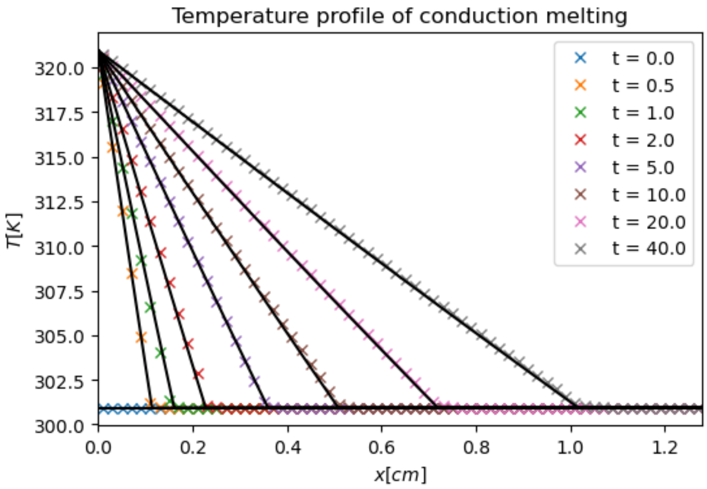

Figure 6.2: Simulated temperature profile vs analytical solution for a 64 × 16 grid and no refinement.

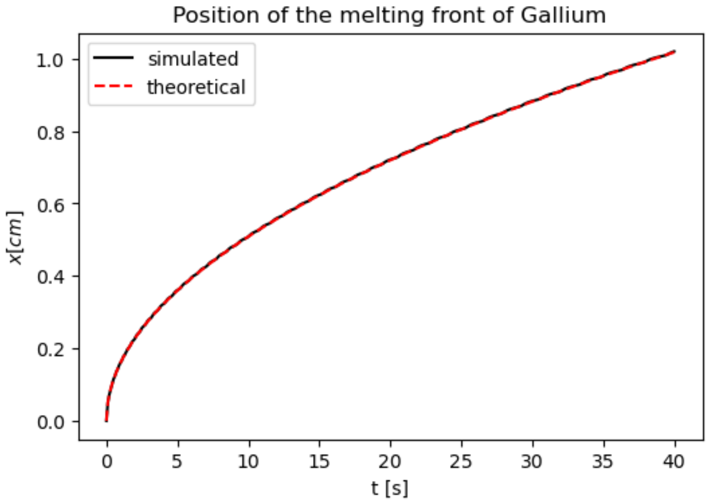

Figure 6.3: Simulated temperature profile vs analytical solution for a 64 × 16 grid and no refinement.

6.1.2 $N_x = 32$, $N_y = 8$, one level of refinement

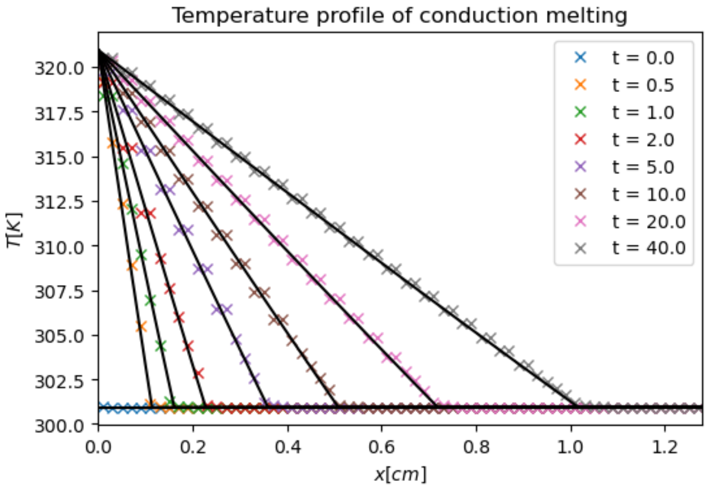

Figure 6.4: Simulated temperature profile vs analytical solution for a 32 × 8 grid and one level of refinement.

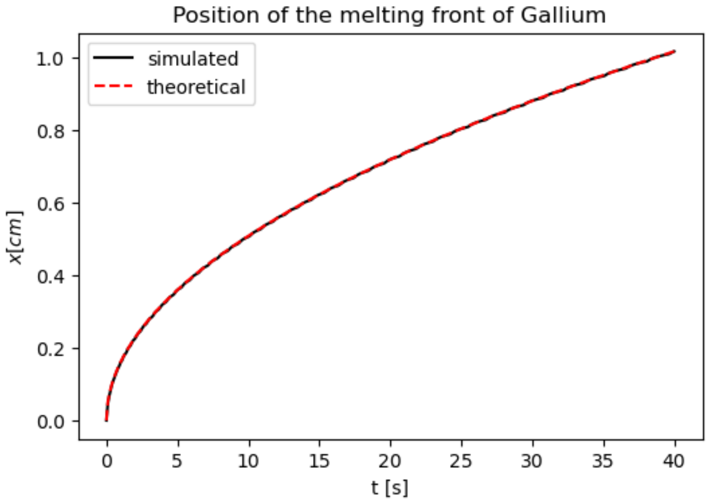

Figure 6.5: Simulated temperature profile vs analytical solution for a 32 × 8 grid and one level of refinement.

6.1.3 $N_x = 32$, $N_y = 8$, no refinement

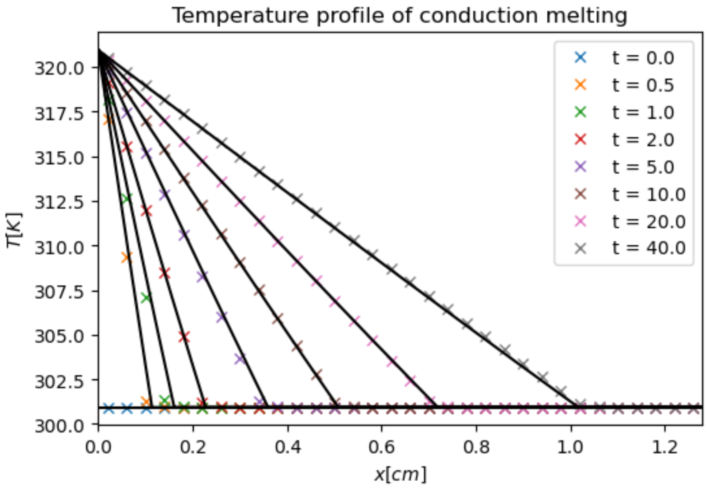

Figure 6.6: Simulated temperature profile vs analytical solution for a 32 × 8 grid and no refinement.

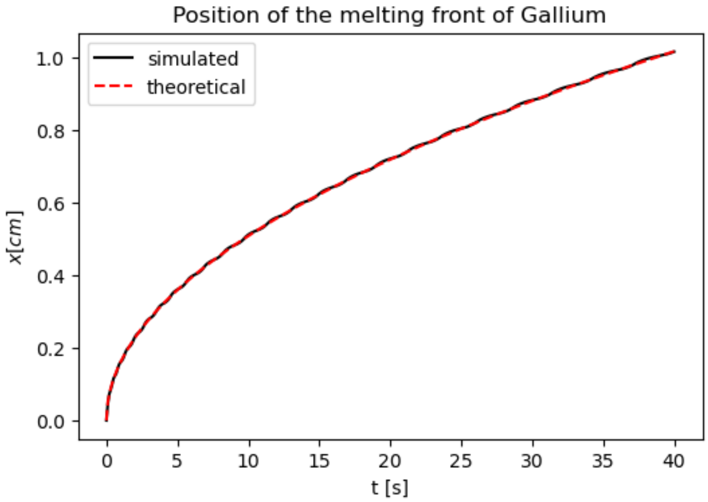

Figure 6.7: Simulated temperature profile vs analytical solution for a 32 × 8 grid and no refinement.

6.1.4 $N_x = 16$, $N_y = 4$, two levels of refinement

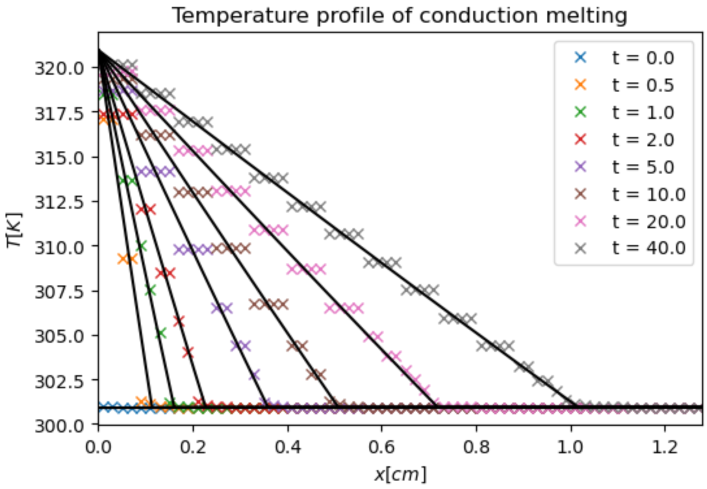

Figure 6.8: Simulated temperature profile vs analytical solution for a 16 × 4 grid and two levels of refinement.

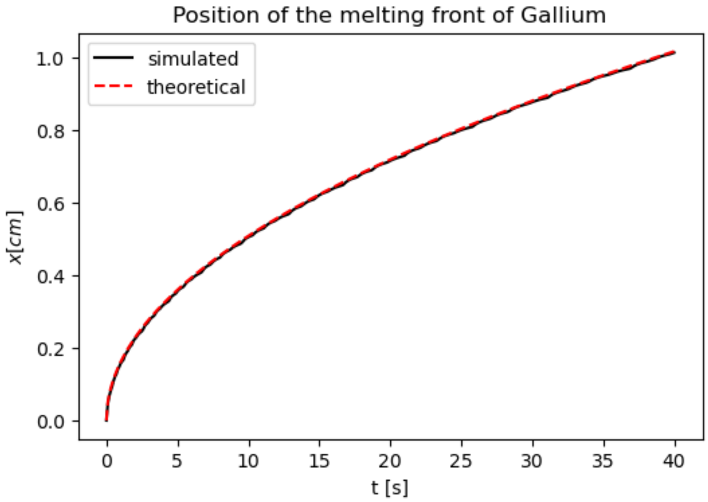

Figure 6.9: Simulated temperature profile vs analytical solution for a 16 × 4 grid and two levels of refinement.

6.1.5 $N_x = 16$, $N_y = 4$, no refinement

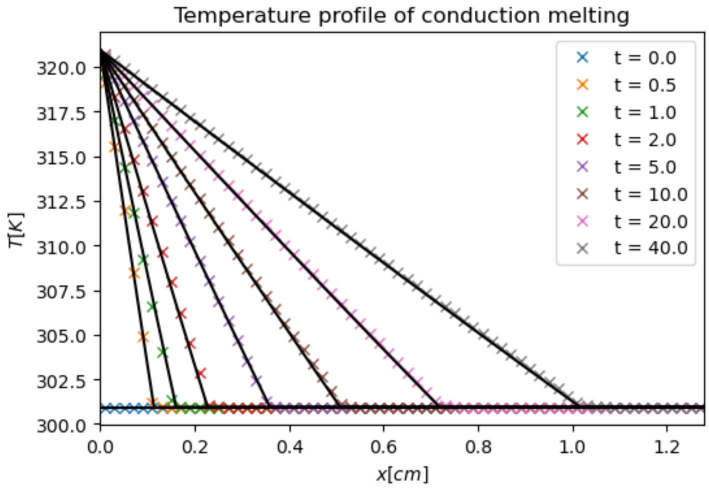

Figure 6.10: Simulated temperature profile vs analytical solution for a 16 × 4 grid and no refinement.

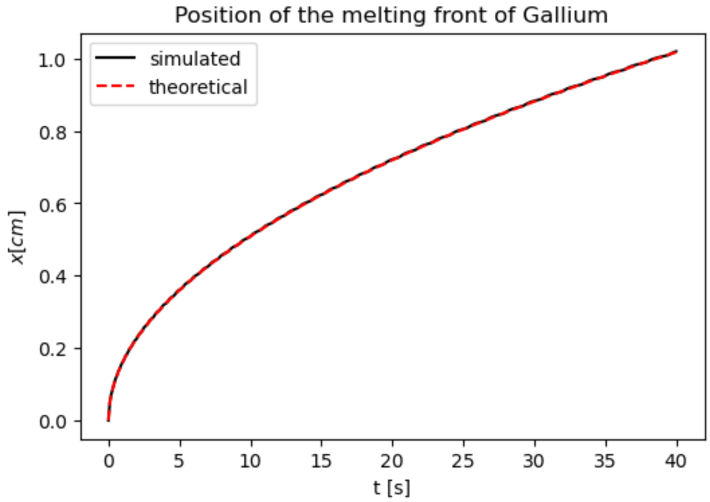

Figure 6.11: Simulated temperature profile vs analytical solution for a 16 × 4 grid and no refinement.